Numerical analysis of flow shedding over an obstacle at low Reynolds number

Gazy F. Al-Sumaily [a,c,*], Hasanen M. Hussen [b], Miqdam T. Chaichan [a], Hayder A. Dhahad [b], Mark C. Thompson [c]

[a] *Energy and Renewable Energies Technology Centre, University of Technology, Iraq*
[b] *Mechanical Engineering Department, University of Technology, Iraq*
[c] *Department of Mechanical and Aerospace Engineering, Monash University, Australia*

ARTICLE INFO

ABSTRACT

This is a numerical investigation of the unsteady mixed convective flow over an isothermally heated circular cylinder. The flow is directed vertically downwards with buoyancy forces in the opposite direction. A parametric analysis was conducted at five Reynolds numbers $Re = 10, 20, 30, 40, 100$, and for Richardson numbers between $Ri = 0$ and 0.5, to evaluate the influence of thermal buoyancy on the instantaneous flow behaviour, vortex-shedding characteristics, thermal fields, and mean heat-transfer rates. The simulations show that at the highest Reynolds number investigated, $Re = 100$, the normal periodic von Kármán vortex street still characterises the flow as Richardson number is increased; however, the oscillation frequency decreases and the oscillation amplitude increases. For $Re \leq 40$, a new vortex street appears, named the "*Buoyancy-Opposing Vortex Street*", due to thermal buoyancy modifying the von Kármán street. Interestingly, at very low $Re = 20$ and 10, the von Kármán street completely disappears in the heated wakes, whereas the "*Buoyancy-Opposing Vortex Street*" remains as the sole vortex street characterising the flow.

1. Introduction

Amongst the most significant flow phenomena to appear when a viscous fluid flows over a bluff body is the von Kármán vortex street consisting of a regular array of shed wake vortices, due to its rich flow physics. The peculiarities of this phenomenon for different-shaped obstacles have been reviewed in several articles, see for example (Bergere and Wille (1972) and Williamson (1996)). The occurrence of vortex shedding can have serious implications, for instance causing strong fluctuating forces that can cause structural fatigue or structural resonance. Therefore, it can useful to be able to exert control to reduce or even enhance this phenomenon (for energy generation devices), by using flow control techniques. There are two established approaches for controlling the flow namely, passive and active methods. For passive methods, flow control is achieved without consuming external energy, employing techniques like splitter plates or adjusting the body shape. However, in active methods, the flow is controlled throughout consuming external energy such as through the application of heating and using thermal buoyancy. Indeed, the case of a heated obstacle positioned normally through a vertical assisted or opposed buoyancy flow is

implemented in thermal applications such as tubes of heat exchangers, fuel rods of nuclear reactors, tubes of heat pumps or cooling systems inside electronic devices, etc. The concept is that thermal buoyancy can cause secondary flows owing to density differences, and inject extra momentum into the boundary layer, adjusting the flow separation and reducing or eliminating the vortex shedding.

When the flow orientation is vertically upwards and passes a heated bluff obstacle, a buoyancy-assisted flow (parallel flow) is produced. Thus, the flow direction is aligned with the direction of the positive buoyancy force. However, if a vertically upward flow passes a cooled obstacle, an opposing-buoyant flow (contra flow) is generated. Hence, although the flow is still oriented vertically upwards, this is opposed by the negative buoyancy force. These two kinds of flows have been considered in many works to study the concept of using thermal buoyancy effects to eliminate vortex shedding.

Oosthuizen and Madan (1970) investigated experimentally mixed convective parallel flow about a circular cylinder for Reynolds numbers ranging between 100–300, in which the flow is quite unstable. However, their attention was given to formulating a correlation for the Nusselt

* Corresponding author.
E-mail addresses: gazy.alsumaily@monash.edu (G.F. Al-Sumaily), hasanen.m.hussen@uotechnology.edu.iq (H.M. Hussen), miqdam.t.chaichan@uotechnology.edu.iq (M.T. Chaichan), hayder.a.dhahad@uotechnology.edu.iq (H.A. Dhahad), mark.thompson@monash.edu (M.C. Thompson).
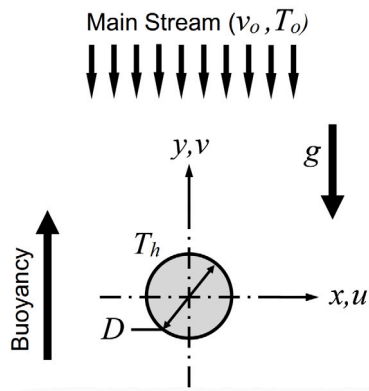
Main Stream (v_o, T_o)

Fig. 1. Physical problem under consideration.

number, not to the characteristics of the near-wake vortices. Jain and Lohar (1979) studied numerically unsteady mixed convection around a circular cylinder at two Reynolds numbers of 100 and 200. They found that the vortex shedding becomes faster in the mixed convection regime introducing further asymmetry in the phenomenon of heat transfer. Farouk and Guceri (1982) analysed natural and mixed convective flows over a hot circular cylinder located inside an insulated plane channel for different Rayleigh numbers. For the case of mixed convection, the cylinder was assumed to face a creeping vertical upward free-stream at low a Reynolds number of 6.20. Interestingly, the results identified a flow reversal occurring in the natural convection mode at the downstream region of the channel. However, in the mixed convection regime, this flow reversal was shown to decrease significantly, and with further increases in Reynolds number, it was shown to vanish entirely. Badr (1984) studied combined convection around a circular cylinder placed in a vertically upward flow considering two cases: when the cylinder is hot (aiding flow) and when the cylinder is cold (opposing flow). The study was performed at low Reynolds numbers (Re = 5, 20, 40) for both cases, and at different Grashof numbers. They observed the formation of twin vortices in the wake region, while in aiding flow, increasing Grashof number delays the flow separation from the cylinder surface. However, in opposing flow, as Grashof number increases, the wake behind the cylinder grows until its boundaries entirely encircles the cylinder making a disk-shaped dome. Inside the dome, the flow circulation is mainly driven by buoyancy effects, not by the background flow momentum, but without triggering of any vortex shedding. The same author (Badr, 1985) considered his prior physical case to examine the influence of the free-stream direction, varying from the vertically upward parallel flow to the vertically downward contra flow. He deduced similar findings as in his previous work, thus, in parallel flow, as Grashof number increases, the flow circulation in the wake region disappears, and the flow separation takes place merely at the rearward stagnation point of the cylinder. However, in contra flow, two distinct zones were observed: in the first zone, the cylinder is surrounded entirely with a circulating flow generated by the effect of buoyancy forces. The second zone is formed around the first one by the effect of background flow, and the buoyancy forces have minimal impact on it as the buoyant flow is never convected into the second zone. Noto and Matsumoto (1987) reported an increase in the vortex shedding frequency with increasing the cylinder temperature inside a parallel flow. However, their study was made only in a transient state well before a fully periodic state was achieved: for $t < 40$. Chang and Sa (1990) and Hatanaka and Kawahara (1995) studied vortex-shedding in the near-wake region of an unbounded heated/cooled circular cylinder positioned inside a vertical free-stream for a Reynolds number of 100. The heated/cooled cylinder surface status was expressed through the positive/negative effect of buoyancy forces. They employed varying numerical techniques, but the two of them found that cooling the

cylinder increases flow periodicity. Nevertheless, heating the cylinder was discovered to restrain the vortex shedding, converting it into a stable flow with double vortices at a certain critical Richardson number of 0.15, extinguishing the wake breakdown into the von Kármán vortex street. Singh et al. (1998) also investigated the impact of buoyancy force on the suppression of vortex shedding at the rear of a hot/cold circular cylinder, but confined it through positioning it inside a vertical channel. The investigation was conducted at constant blockage ratio of 0.25, but at a similar Reynolds number of 100. They also concluded that the flow is still characterised by a vortex street until the Richardson number approached the value of 0.15; although, thereafter, the assisting buoyancy completely changes the flow dynamics by causing shedding to cease. Sharma and Eswaran (2004) investigated the impact of negative and positive buoyancy forces on thermal and flow peculiarities of a square cylinder in a vertically upward flow at a constant Reynolds number of 100. Similar to the case of the circular cylinder, the Kármán vortex street was observed to collapse in the parallel buoyant flow at the same critical Richardson number of 0.15. The same authors, Sharma and Eswaran (2005), examined the influence of confining a square cylinder on vortex shedding suppression for different blockage ratios of 0.1, 0.3, 0.5. This study was also performed for heated/cooled cylinders in vertically upward flow at Re = 100. It was observed that increasing the blockage ratio decreases the value of the critical Richardson number required for vortex shedding suppression. However, this effect was found to occur up to blockage ratio of 0.3, but for greater values, the critical Richardson number starts to increase. Noto and Fujimoto (2007) tested the influence of buoyancy forces on the wake three-dimensionality and vortex dislocations, as well as on Kármán vortex shedding, in the heated wake region of a circular cylinder installed inside a vertical airstream. The study was performed at constant Reynolds number of 300 and Richardson number of 0.3. They reported generating flow three-dimensionality in the hot wake region and noted the occurrence of vortex dislocations. It was also reported that buoyancy forces can easily restrain three-dimensionality and suppress vortex dislocation. Noto and Sugimura (2007) investigated the effect of strong cooling (negative buoyancy) of a circular cylinder placed inside a vertically upwards directed airstream on generating vortex shedding for a low range of Reynolds number (Re = 15 − 44). Interestingly, their results showed the occurrence of a new vortex street called the "Cooled Vortex Street" at these low Reynolds numbers. They claimed that the consistent rolling up of flow shear layers is observed in both the Kármán and Cooled Vortex Streets, but it is greatly larger in the latter. Singh et al. (2007) conducted experimental work to investigate the effect of buoyancy on the vortex shedding behind cylinders of both square and circular cross-sections in vertical parallel flow for Reynolds number ranging between 53 and 118, and Richardson number between 0.025 and 0.314. They used Schlieren Image Visualisation (SIV) to observe the suppression of vortex shedding through the effect of cylinder heating. It was found that the frequency of vortex shedding is a function of Reynolds and Richardson numbers. Thus, it was seen that the shedding frequency is increased by increasing Richardson number due to the assisting buoyancy effects. However, the shedding stops abruptly, and its frequency becomes zero at and beyond a critical Richardson number, which was also found to be a function of Reynolds number. Gandikota et al. (2010) also studied the impact of assisting buoyancy effects on parallel flow on the excitation and suppression of vortex shedding for a heated/cooled circular cylinder placed within a vertical duct. The study was conducted for Reynolds numbers of 50–150, and at two blockage ratios of 0.02 and 0.25. They found that the blockage ratio changes the value of the critical Richardson number. Thus, it was shown that at Re = 100, the vortex stops shedding at critical Richardson numbers of 0.15 and 0.18 at blockage ratios of 0.25 and 0.02, respectively. That is, higher critical Richardson number occurs for lower blockage ratio. Chatterjee and Mondal (2012) studied the influence of positive/negative buoyancy effects on the flow structure around a confined square cylinder located
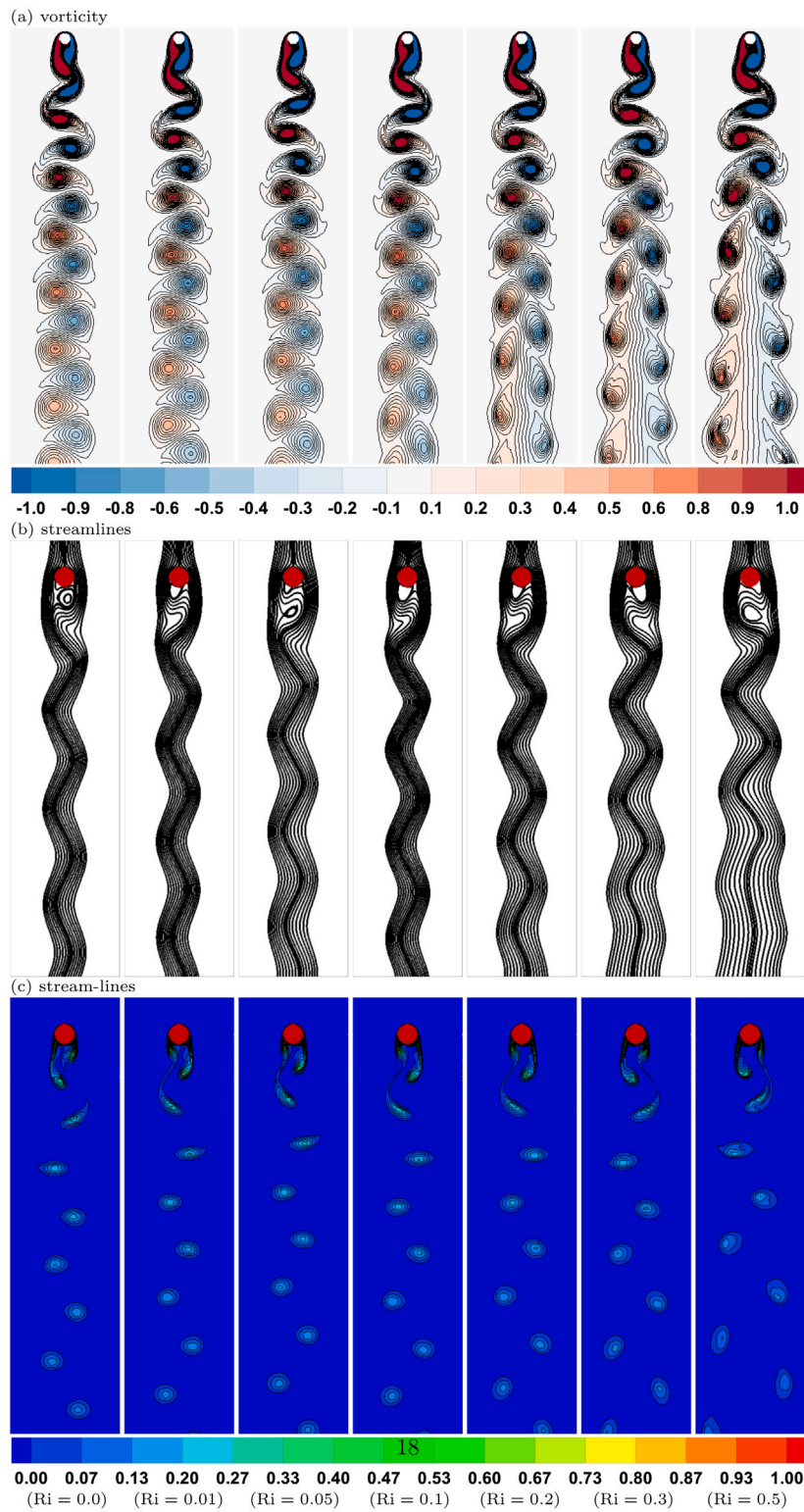
Fig. 2. Non-dimensional patterns of (a) vorticity, (b) streamlines, (c) iso-therms, at Re = 100, for different Ri = 0 − 0.5. (For interpretation of the references to colour in this figure legend, the reader is referred to the web version of this article.)

within a vertical upward flow. Their study was undertaken for Reynolds numbers varying between 50 and 150, and for two channel blockage ratios of 0.02 and 0.25. They reported that in the negative buoyancy case, the opposing buoyant flows are completely distinguished with vortex shedding for all negative Richardson numbers, and for both blockage ratios. However, in the positive buoyancy case, the periodic

flows were shown to become steady, e.g., the vortex shedding discontinues completely, at critical Richardson numbers of 0.25 and 0.2 at the two blockage ratios of 0.02 and 0.25, respectively. Patel et al. (2018) carried out a numerical study to investigate the flow dynamics and thermal response around two side-by-side square cylinders at incidence in a vertically upward bounded airstream. They studied the effect of assisting buoyancy via altering the Richardson number between 0 and
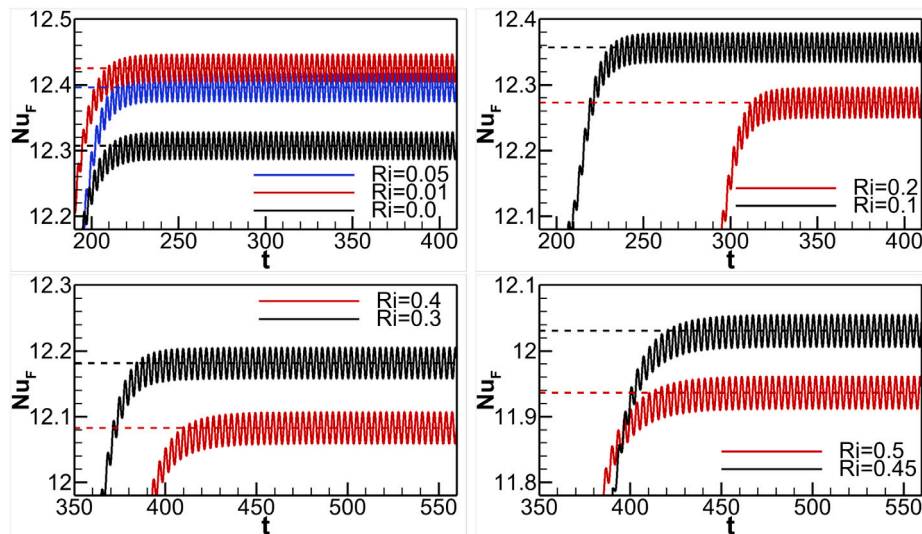
Fig. 3. Variation of Nu_F with time at Re = 100, for different Ri = 0 − 0.5.

1, at constant a Reynolds number of 100. They also tested the impact of changing the incidence angle by rotating the cylinders between 0° and 45° clockwise or counter-clockwise, individually or simultaneously. The results showed that when buoyancy effects are not superimposed, the vortex shedding occurred at every incidence angle. However, when the buoyancy effects are superimposed, the vortex shedding was shown to be suppressed. Also, the capability of Richardson number to restrain the vortex shedding was found to increase with increasing the incidence angle, which also enhances the frequency of vortex shedding. Salimipour (2019) researched employing the buoyancy-assisted flow technique to suppress undesirable vortex shedding generated behind a circular cylinder subjected to a vertical unbounded airflow at Reynolds number of 200. The cylinder was heated, either fully or partially, at the top and the remaining part was assumed to be insulated. The results showed that when the cylinder is fully heated, there exists a critical Grashof number for eliminating vortex shedding. However, when the cylinder is partially heated, there is an optimal surface heating angle, depending of the value of Grashof number, for stopping the vortex shedding and getting the lowest drag coefficient. Al-Sumaily et al. (2020) examined the influence of buoyancy effects on the vortex shedding of an unconfined circular cylinder placed within a vertically upward stream for different values of Reynolds number between 20 − 150. As they used water as the working fluid. High values of Richardson number, up to 5.0, were considered to explore strong thermal buoyancy effects on the system. The results revealed that the strength of vortex shedding increases by the initial effect of thermal buoyancy. However, as heating is increased, vortex shedding stops abruptly, and the otherwise dynamic wake was found to degenerate into steady double vortices at a certain critical Richardson number, which was observed to increase as Reynolds number was increased.

In contrast, when the flow orientation is vertically downward passing a heated bluff obstacle, directly opposing forced and free convective flows are generated. In the literature, this case has been given less attention so far, possibly by reason of computational instability, particularly when inertia and buoyancy forces have analogous magnitudes. Hatton et al. (1970), Oosthuizen and Madan (1971) and Nayak and Sandborn (1977) conducted pioneering experimental works to study directly opposed forced and free convection flows around a heated circular cylinder. Hatton et al. (1970) investigated the effect of free-stream direction for low Reynolds numbers up to 45. They suggested a correlation that fitted the data reasonably well except for the case when the forced flow approached a direction opposite to that of natural convection. Oosthuizen and Madan (1971) investigated similar effect when the forced flow makes an angle of 0°, 90°, 135° or 180° with

the direction of natural convection, but for higher Reynolds numbers ranging between 100 − 300, in which the flow is highly unsteady. However, their concern was calculating the average Nusselt number, not in the detailed behaviour of the near-wake vortices. Based on flow visualisation and measurements of heat transfer, Nayak and Sandborn (1977) observed three flow modes. At very low Reynolds number, a free convection buoyant plume flow predominates the system. At a lower critical Reynolds number, when the forced flow has almost a similar order of magnitude as free-buoyant flow, a periodic heat transfer was established. At an upper critical Reynolds number, the periodic heat transfer stops suddenly, and after that a steady flow was established. Later, Martínez-Suástegui and his co-workers (Guillén et al., 2014; Salcedo et al., 2017; Saldaña et al., 2019; Sáchica et al., 2022) investigated experimentally and numerically opposing downward mixed convective water flow around confined single and double circular cylinders under different flow and heating conditions. Almost those works, Guillén et al. (2014) conducted an experimental study using Particle Image Velocimetry (PIV) to image vertical downward opposing flows over a hot cylinder positioned inside a perpendicular channel, to assess the buoyancy effects on vortex shedding. The experiments were performed at constant Reynolds number of 170, channel blockage ratio of 0.287, and for Richardson numbers ranging between −1 ≤ Ri ≤ 5. The results showed that at Ri = −1, the buoyancy-assisting flow postpones the flow separation around the cylinder wall, suppressing entirely the vortex shedding, consequently the occurrence of any *Kármán* vortex street collapses. However, at Richardson number Ri = 0 and 1, oscillatory periodic flows are occurred, displaying a regular stable von *Kármán* vortex street. It was shown that increasing Richardson number from 0 to 1 shortens the wake length promoting an early flow separation and decreases slightly the shedding frequency. For, higher Richardson number Ri ≥ 2, the vortex shedding formed in the backward region of the cylinder becomes strongly unstable owing to the struggle between the downward forced flow and the strong opposing buoyant flow. In addition, the effect of the channel blockage ratio was found to influence positively the value of the oscillation frequency of the vortex shedding, compared with the case of unconfined cylinder. Salcedo et al. (2017) presented numerical results for downward opposing flows crossing two isothermal circular cylinders in a tandem configuration bounded by two vertical plates. They examined the effect of thermal buoyancy, for Richardson number of −1 ≤ Ri ≤ 4, for cases with a gap between cylinders, for three pitch-to-diameter ratios of 2, 3, 5, on the flow dynamics and thermal response at fixed Reynolds number of 200, and blockage ratio of 0.2. It was reported that depending on the buoyancy strength and the gap width, five well-defined flow models are identified
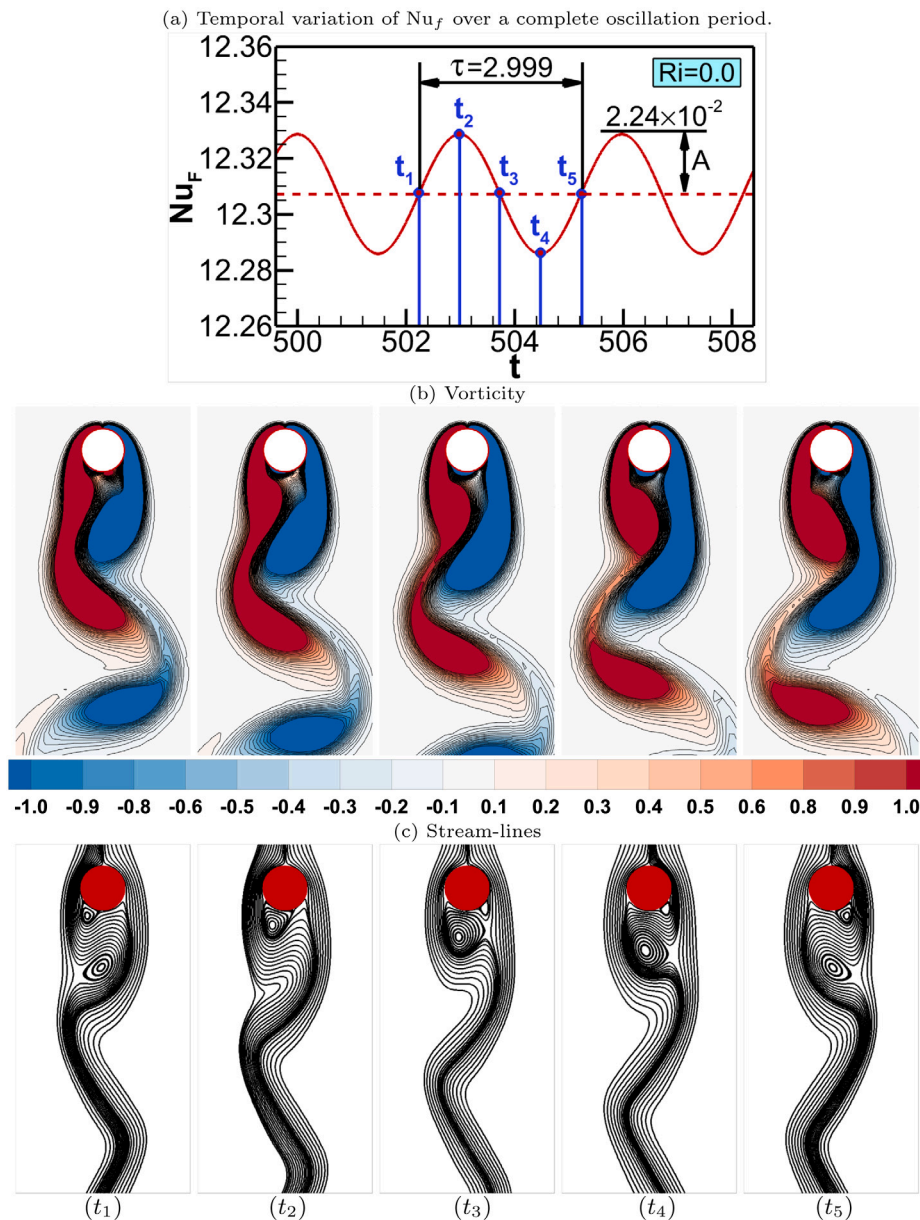
(a) Temporal variation of Nu_f over a complete oscillation period.

(b) Vorticity

(c) Stream-lines

(t_1) $\quad$ (t_2) $\quad$ (t_3) $\quad$ (t_4) $\quad$ (t_5)

Fig. 4. (a) Transient oscillatory behaviour of Nu_f, (b) and (c) patterns of vorticity and streamlines, respectively, for five instant times over a complete oscillation period, at Re = 100 and Ri = 0.

as follows: stable flow, oscillatory periodic, oscillatory quasi-periodic, bi-stable flow, and chaotic flow. Saldaña et al. (2019) performed an experimental investigation into mixed convection downward flows about a cylinder bounded by a vertical closed-loop rectangular duct. The investigation was made for high Richardson number between 3.6 and 142.5, and for Reynolds number changing between 170 and 260, at fixed blockage ratio of 0.4. In this study, they only evaluated the influence of positive thermal buoyancy on the variations of cylinder surface temperature and the average heat transfer from the cylinder. Recently, Sáchica et al. (2022) explored the vortex suppression past a confined circular cylinder under mixed convection in magnetohydrodynamic nano-fluid flows. Laidoudi and Bouzit (2018) carried out a numerical study to comprehend the impacts of opposing/assisting thermal buoyancy forces on a steady mixed convective downward flow crossing a circular cylinder bounded by two vertical plates. The study was conducted for low Reynolds numbers between 5 and 40, for negative and positive Richardson numbers between −1 and 1, at fixed Prandtl number of 1 and blockage ratio of 0.2. They numerically

solved the steady-state equations; therefore, they could not capture the transient behaviour of the flow dynamics behind the cylinder.

Through this discussion of the literature, it appears that the identified investigations have not reported how opposing forces due to positive buoyancy effects are likely to influence the vortex structure of a vertical downward flow over a heated circular cylinder at intermediate Reynolds numbers, particularly when the buoyant forces are of the same order of magnitude as the inertia forces. In addition, for this kind of downward opposing flow over a hot circular cylinder, the existing literature did not show if the phenomenon of vortex shedding can be triggered in a low range of Reynolds number, i.e., between 20 and 40, where the natural wake contains only twin steady attached vortices. It is perhaps worth reiterating that only the study of Noto and Sugimura (2007) investigated the impact of negative buoyancy by cooling a circular cylinder within a vertically upward airstream, to discover the possibility of triggering a new type of vortex street at low Reynolds numbers of (Re = 15 − 44). Therefore, the current numerical study was conducted to address these open issues and further explore the effect of
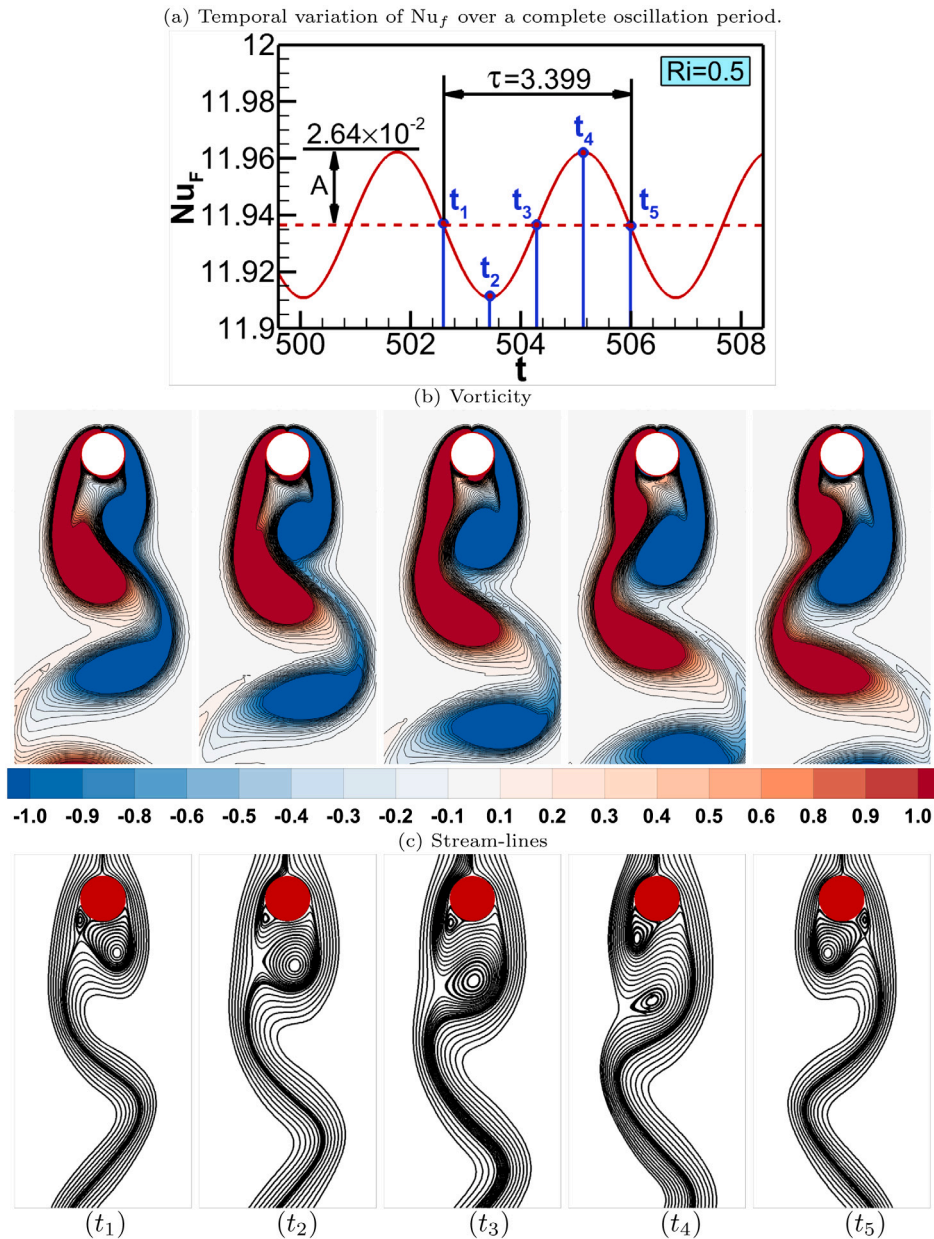
(a) Temporal variation of Nu_f over a complete oscillation period.

(b) Vorticity

(c) Stream-lines

Fig. 5. (a) Transient oscillatory behaviour of Nu_f, (b) and (c) patterns of vorticity and streamlines, respectively, for five instant times over a complete oscillation period, at Re = 100 and Ri = 0.5.

opposing buoyancy on these contra flows and particularly the detailed wake characteristics.

2. Physical problem

Fig. 1 displays a schematic of the geometry of the problem under consideration along with the Cartesian coordinate system employed. The configuration consists of a fixed circular cylinder of size (D), isothermally heated to maintain a constant temperature of (T_h), and exposed to a vertically downward flow with velocity v_o and lower temperature T_o.

3. Mathematical formulation

In this analysis, water is assumed to be the working fluid with Prandtl number Pr = 7.1. The fluid is incompressible, viscous and New-tonian, with other properties constant except density for the buoyancy term, which is modelled using the Boussinesq approximation. Although

fluid viscosity is typically a function of temperature, this dependence is neglected here. In addition, the cylinder length is assumed to be long enough so that end effects do not influence the flow in the central spanwise region, and thus the problem becomes two dimensional. Also, the flow is considered to be laminar and two dimensional, consistent with low Reynolds numbers considered in the present investigation. Thus, the non-dimensional form of the standard mass, momentum, and energy equations expressed in Cartesian coordinates can be written as follows (Al-Sumaily et al., 2020):

$$\frac{\partial U}{\partial X} + \frac{\partial V}{\partial Y} = 0, \tag{1}$$

$$\frac{\partial U}{\partial t} + U\frac{\partial U}{\partial X} + V\frac{\partial U}{\partial Y} = -\frac{\partial P}{\partial X} + \frac{1}{\text{Re}}\left(\frac{\partial^2 U}{\partial X^2} + \frac{\partial^2 U}{\partial Y^2}\right), \tag{2}$$

$$\frac{\partial V}{\partial t} + U\frac{\partial V}{\partial X} + V\frac{\partial V}{\partial Y} = -\frac{\partial P}{\partial Y} + \frac{1}{\text{Re}}\left(\frac{\partial^2 V}{\partial X^2} + \frac{\partial^2 V}{\partial Y^2}\right) + \text{Ri }\theta, \tag{3}$$

$$\frac{\partial \theta}{\partial t} + U\frac{\partial \theta}{\partial X} + V\frac{\partial \theta}{\partial Y} = \frac{1}{\text{Re.Pr}}\left(\frac{\partial^2 \theta}{\partial X^2} + \frac{\partial^2 \theta}{\partial Y^2}\right), \tag{4}$$

(a) oscillation frequency

Re=100

Karman Street

(b) oscillation amplitude

Re=100
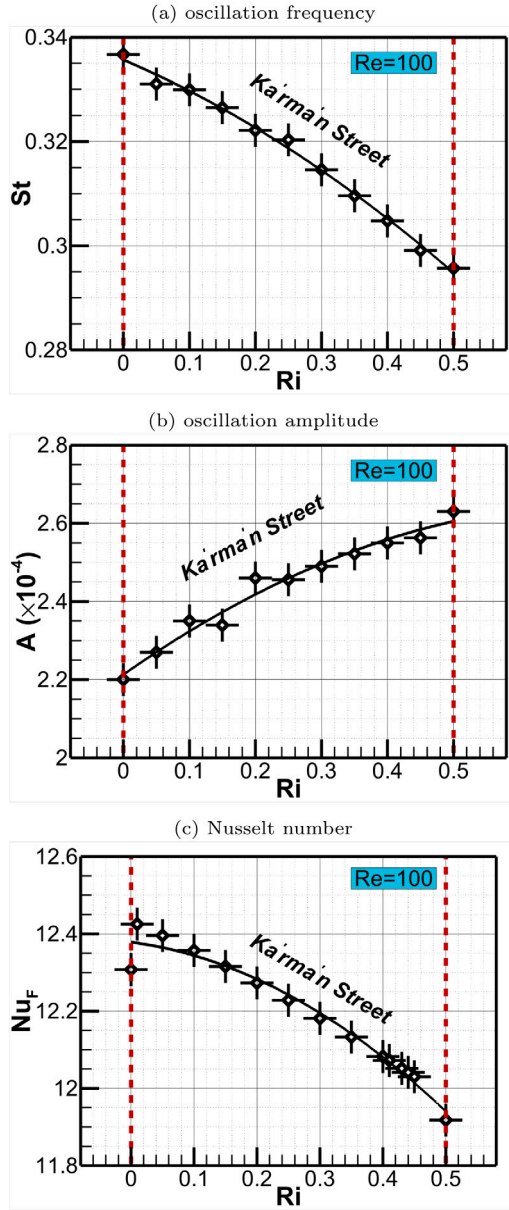
Karman Street

(c) Nusselt number

Re=100

Karman Street

Fig. 6. Variation of (a) Strouhal number, (b) oscillation amplitude, (c) average Nusselt number, with Ri, at Re = 100.

where (U, V, P, θ), and t are the dimensionless flow velocity components, kinematic pressure, temperature, and time. It can be seen that the flow is governed by three parameters, namely the Reynolds number (Re), Richardson number (Ri), and Prandtl number (Pr), which can be expressed as:

$$\text{Re} = \frac{U_\infty D}{\nu}, \quad \text{Ri} = \frac{\text{Gr}}{\text{Re}^2}, \quad \text{Pr} = \frac{\nu}{\alpha}, \quad \text{and} \quad \text{Gr} = \frac{g\beta D^3(T_h - T_o)}{\nu^2}. \quad (5)$$

Here, β is the volumetric expansion coefficient, Gr is Grashof number, g is the gravitational acceleration, U_∞ is the inflow speed, and ν and α are the kinematic viscosity and the thermal diffusivity of the fluid, respectively.

4. Initial and boundary conditions

The initial velocity and temperature fields were set to zero ($U = V = \theta = 0$) at $t = 0$. For $t > 0$, before evolving the numerical solution,

the following conditions were set at the boundaries:

at the inlet, $\quad U_o = 0, \quad V_o = -1, \quad \theta_o = 0,$

at the outlet, $\quad \dfrac{\partial U}{\partial Y} = \dfrac{\partial V}{\partial Y} = \dfrac{\partial \theta}{\partial Y} = 0,$

at the lateral boundaries, $\quad \dfrac{\partial U}{\partial X} = \dfrac{\partial V}{\partial X} = \dfrac{\partial \theta}{\partial X} = 0,$

at the cylinder solid wall, $\quad U = V = 0, \quad \theta_h = 1. \quad (6)$

From the predicted non-dimensional flow field, the non-dimensional stream function (Ψ), which depicts the fluid movement, is computed by:

$$U = \frac{\partial \Psi}{\partial Y}, \quad \text{and} \quad V = -\frac{\partial \Psi}{\partial X}. \quad (7)$$

Then, the non-dimensional vorticity (Ω), which describes the local rotation of the flowing fluid, is computed from the stream function by:

$$-\Omega = \frac{\partial^2 \Psi}{\partial^2 X} + \frac{\partial^2 \Psi}{\partial^2 Y}, \quad (8)$$

where, $(\Omega = \omega D/v_o)$, and (ω) is the dimensional vorticity. In addition, from the predicted non-dimensional thermal field, the heat transfer from the heated cylinder to the surrounding fluid is then calculated and quantified through the Nusselt number:

$$\text{Nu}_F = \frac{1}{S} \int_0^{\mathbf{S}} \left(-\frac{\partial \theta}{\partial \mathbf{n}}\right) \cdot d\mathbf{s}. \quad (9)$$

Here, Nu_F is the surface-averaged fluid Nusselt number, S is the cylinder circumference, $\mathbf{n}$, and $\mathbf{s}$ are the surface normal and tangential unit vectors, respectively.

5. Numerical solution

The spectral-element method is used to discretise the governing Eqs. (1)–(4) in space. This is basically a high-order finite-element method where the computational domain is split up into a number of quadrilateral macro-elements or cells, which are further subdivided internally using a Lagrange polynomial expansion to capture the variation of the flow and thermal variables. The approach is fully described in Karniadakis and Sherwin (2005). A time-splitting approach, described below, is used to discretise the equations in time (Karniadakis et al., 1991; Thompson et al., 2006). The combined flow/heat transfer equations are integrated in our existing in-house numerical code for analysing unsteady momentum and energy transport in the mixed convection regime. Further brief details and relevant references are provided below.

5.1. Temporal discretisation

This technique is a three-step time-splitting scheme used to advance the solution in time. After rearranging the Eqs. (2)–(4), the right-hand side of each equation is split into (up to) three terms namely: advection, diffusion, and pressure, with the effect of each term treated separately. In combination, this three (sub-)step integration process leads to overall integration through one time-step. For instance, to discretise the momentum equations ((2),(3)), they are first rearranged as follows:

$$\frac{\partial \mathbf{U}}{\partial t} = -(\mathbf{U} \cdot \nabla)\mathbf{U} + \frac{1}{\text{Re}}\left(\nabla^2 \mathbf{U}\right) - \nabla P. \quad (10)$$

Then, the non-linear advection term is integrated through the whole time-step, generating an intermediate velocity field ($\mathbf{U}^{(\star)}$):

$$\mathbf{U}^{(\star)} - \mathbf{U}^{(n)} = -\int_t^{t+\Delta t} \left((\mathbf{U} \cdot \nabla)\mathbf{U}\right) dt, \quad (11)$$

where, (n) represents the present time-step. Next, this first intermediate velocity is used as an initial value for integrating the pressure term, generating another intermediate velocity field ($\mathbf{U}^{(\star\star)}$):

$$\mathbf{U}^{(\star\star)} - \mathbf{U}^{(\star)} = -\int_t^{t+\Delta t} \left(\nabla P\right) dt. \quad (12)$$
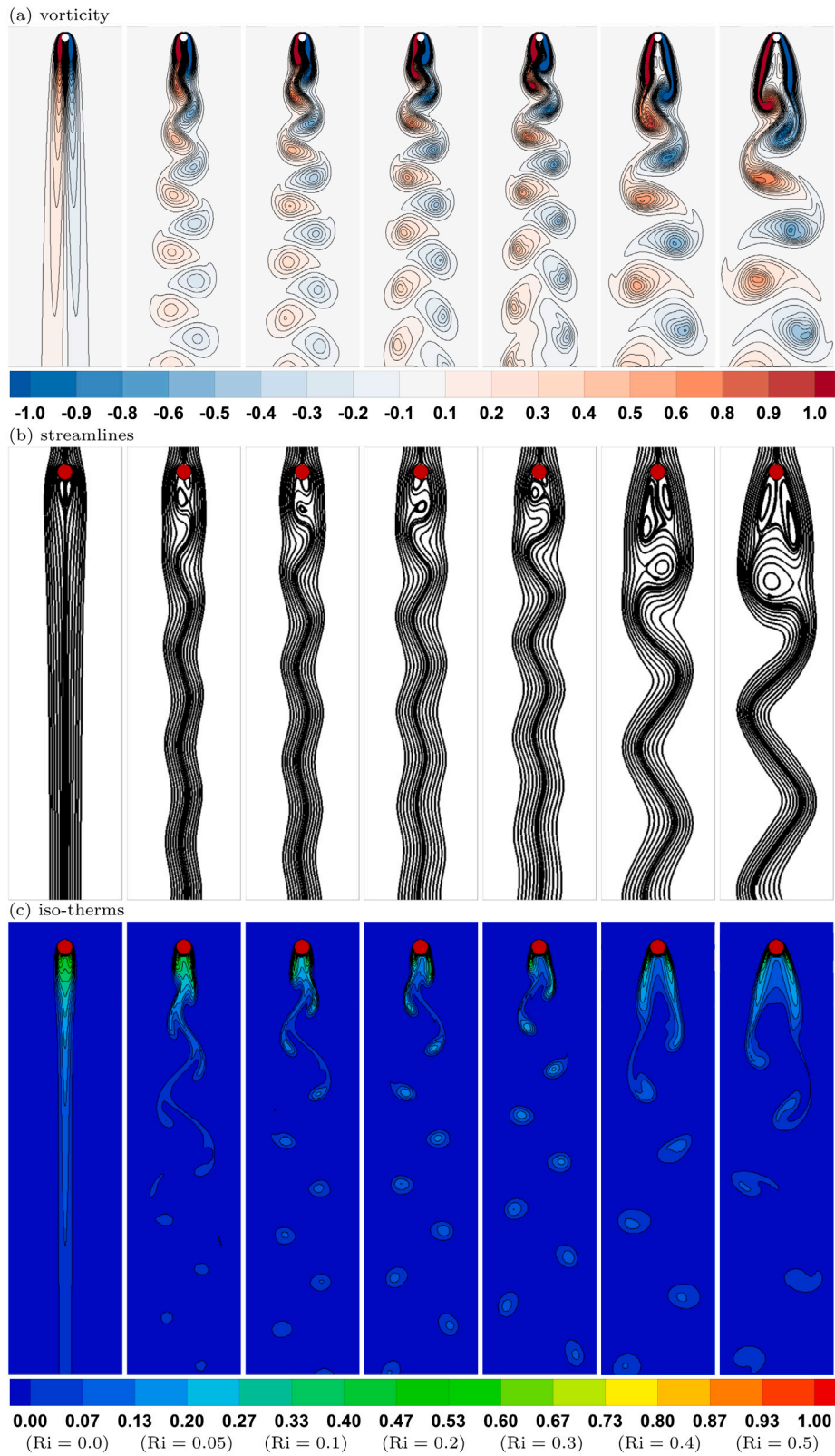
(a) vorticity

(b) streamlines

(c) iso-therms

Fig. 7. Patterns of (a) vorticity, (b) streamlines, (c) iso-therms, at Re = 40, for different Ri = 0 − 0.5.
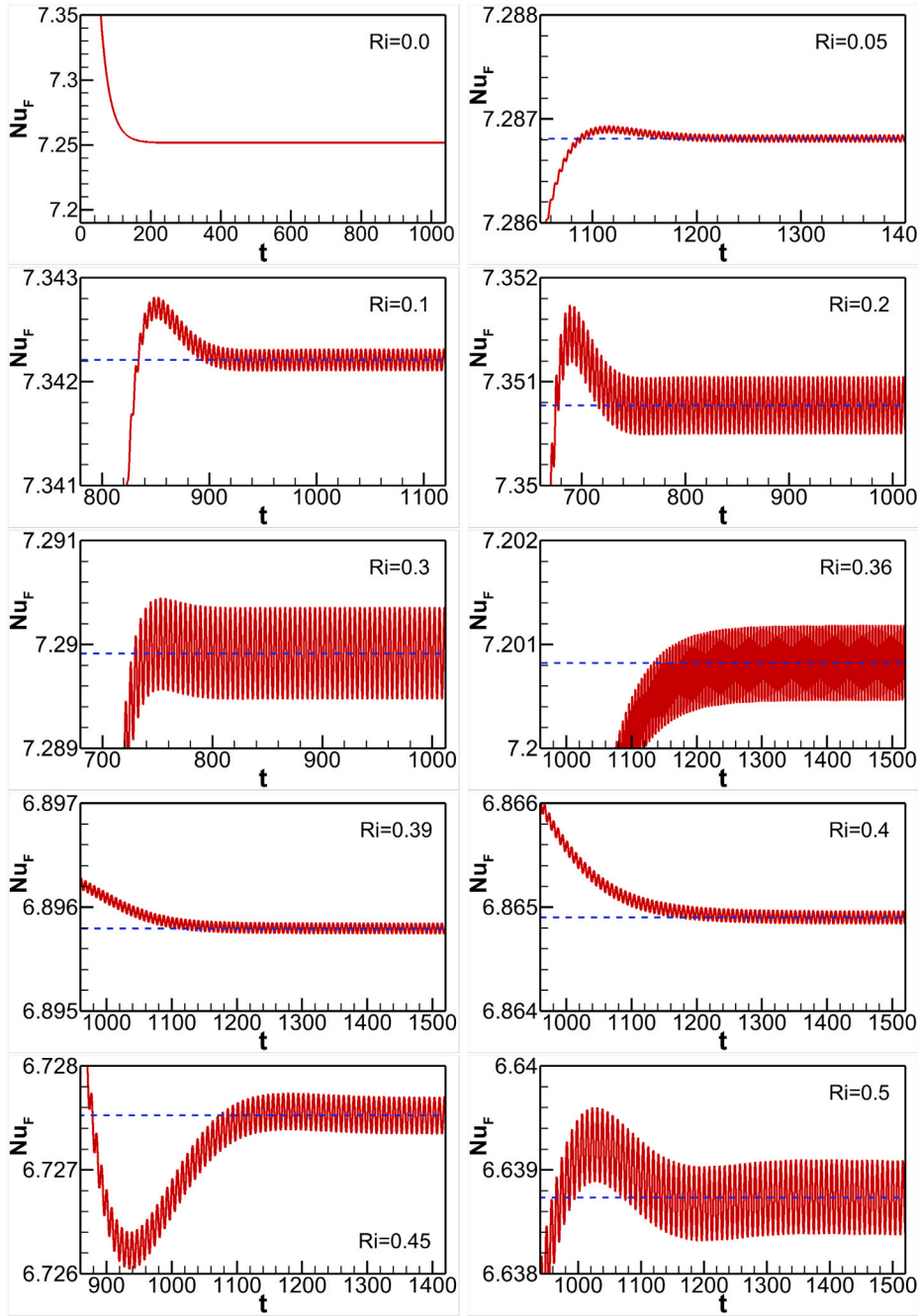
Fig. 8. Variation of Nu_F with time at $\mathrm{Re} = 40$, for different $\mathrm{Ri} = 0 - 0.5$.

Finally, this intermediate secondary velocity is employed as an initial value for integrating the diffusion term, for obtaining the final velocity field $\left(\mathbf{U}^{(n+1)}\right)$ at the end of the time-step:

$$\mathbf{U}^{(n+1)} - \mathbf{U}^{(\star\star)} = \frac{1}{\mathrm{Re}} \int_t^{t+\Delta t} \left(\nabla^2 \mathbf{U}\right) dt, \tag{13}$$

where, $(n + 1)$ represents the next time-step.

In 1st time sub-step, the non-linear advection term in Eq. (11) is approximated employing the second-order Adams–Bashforth approach:

$$\mathbf{U}^{(\star)} - \mathbf{U}^{(n)} = -\Delta t \left(\frac{3}{2} \left((\mathbf{U} \cdot \nabla)\mathbf{U}\right)^{(n)} - \frac{1}{2} \left((\mathbf{U}.\nabla)\mathbf{U}\right)^{(n-1)} \right), \tag{14}$$

where, (Δt) is the time interval. In 2nd time sub-step, the pressure equation (12) is handled in two stages as there are two unknowns. First, the equation is approximated to second-order by

$$\mathbf{U}^{(\star\star)} - \mathbf{U}^{(\star)} = -\Delta t \, \nabla P^{(n+\frac{1}{2})}. \tag{15}$$

Second, the divergence of Eq. (15) is taken, and imposing the continuity condition using Eq. (1) on the second intermediate velocity, results in a Poisson equation of the pressure,

$$\nabla^2 P^{(n+\frac{1}{2})} = \frac{1}{\Delta t} \nabla \cdot \mathbf{U}^{(\star)}. \tag{16}$$

By substituting Eq. (16) into Eq. (15), the velocity $\left(U^{(\star\star)}\right)$ at the end of 2nd time sub-step is calculated. In 3rd time sub-step, the last velocity $\left(U^{(n+1)}\right)$ is estimated by integrating the diffusion term in Eq. (13) using
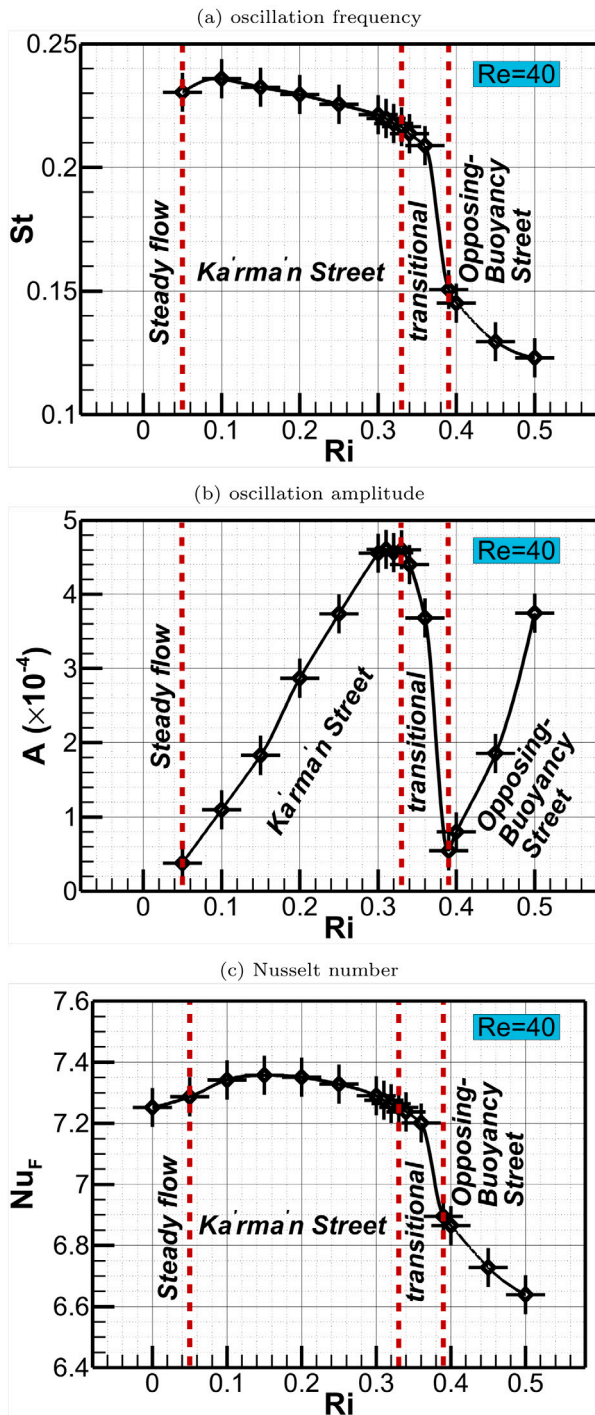
Fig. 9. Variation of (a) Strouhal number, (b) oscillation amplitude, (c) average Nusselt number, with Ri, at Re = 40.

the implicit second-order Adams–Moulton (Crank-Nicholson) approach:

$$\mathbf{U}^{(n+1)} - \mathbf{U}^{(\star\star)} = -\frac{\Delta t}{2\text{Re}}\left(\left(\nabla^2 U\right)^{(n+1)} + \left(\nabla^2 U\right)^{(n)}\right). \tag{17}$$

Further details of this procedure are provided in Karniadakis et al. (1991) and Thompson et al. (2006), including implementation of boundary conditions for the sub-steps.

5.2. Spatial discretisation

Prior to integrating the equations in time, it is necessary to discretise them in space. This is done using a nodal-based spectral-element technique, which is a version of the Galerkin finite-element method. First, the computational domain is subdivided coarsely into a series of macro-elements. This macro-element mesh can be refined in areas that are subject to high gradients, such as boundary layers or shear layers. This process is called *h-refinement*. Within each element, the functional variations of the calculated fields are represented using a tensor product of Lagrange interpolating polynomial expansions. The nodal points used for this representation are chosen to be the integration points of Gauss–Legendre–Lobatto quadrature, which allows the weighted residual integrals resulting from the application of the Galerkin approach to generate the discrete equations, to be evaluated efficiently and accurately. Thus, once a satisfactory grid of macro-elements has been generated, spatial resolution can be increased by increasing the order of the Lagrange polynomial series within each macro-element. This corresponds to increasing the number of internal nodes within elements. This is called *p-refinement*. Importantly, *p-refinement* leads to exponential or spectral convergence as the order of the interpolating polynomials is increased. Importantly, the polynomial order can be chosen at runtime, which means spatial resolution studies can be undertaken using the same macro-element mesh.

In the present implementation, all elements have to be quadrilateral, although they can have curved sides to match the curvature of boundary segments. Details of the approach and implementation applied to the incompressible Navier–Stokes equations are given in Karniadakis and Sherwin (2005), and previous publications on relevant applications including Thompson et al. (2006, 1996), Sheard et al. (2003), Leontini et al. (2007) and Ryan et al. (2005).

This code was used in our previous study (Al-Sumaily et al. (2020)) to analyse a closely related problem of mixed convective flow around an unconfined cylinder, but inside a vertical upward stream. In that study, multiply verification/validation checks were performed against experimental, analytical, and numerical data previously published by Nasr et al. (1994), Cheng (1982), and Buyruk (2002), respectively. It is also worth noting that the implementation has been validated many times previously for different but related problems. For example, it was validated against results from Al-Sumaily et al. (2012) and Al-Sumaily and Thompson (2013) for forced convection flow around a sole cylinder, and against Al-Sumaily (2014) for forced convection flow around multi-cylinders, and with Al-Sumaily and Thompson (2014) for free convection flow over a single cylinder. Thus, for further details on the approach and implementation, the reader is referred to these and previously mentioned publications.

In the following section, attention is given to the numerical predictions that attempt to answer the research questions posed in the introduction.

6. Results and discussion

Numerical simulations of mixed convective contra-flows around an unbounded heated circular cylinder in a vertically downward stream were conducted at five low to moderate Reynolds numbers of Re = 10, 20, 30, 40, 100, and for a range of heating conditions defined through the Richardson number that was varied in the range $0 \leq$ Ri ≤ 0.5 for each Reynolds number. The buoyancy effects on the flow pattern, temperature distribution, and convection heat transfer, are investigated. The flow patterns are represented by vorticity and streamlines, while the temperature distribution is represented by isothermal contours. In this regard, for the vorticity colour map, red indicates counterclockwise rotation (positive vorticity), blue clockwise rotation (negative vorticity), while white indicates a low or zero fluid rotation. For the temperature colour map, red/blue denote hot/cold temperature, respectively. For the latter, the temperature field has been scaled to lie between $\theta = 1$ and 0.
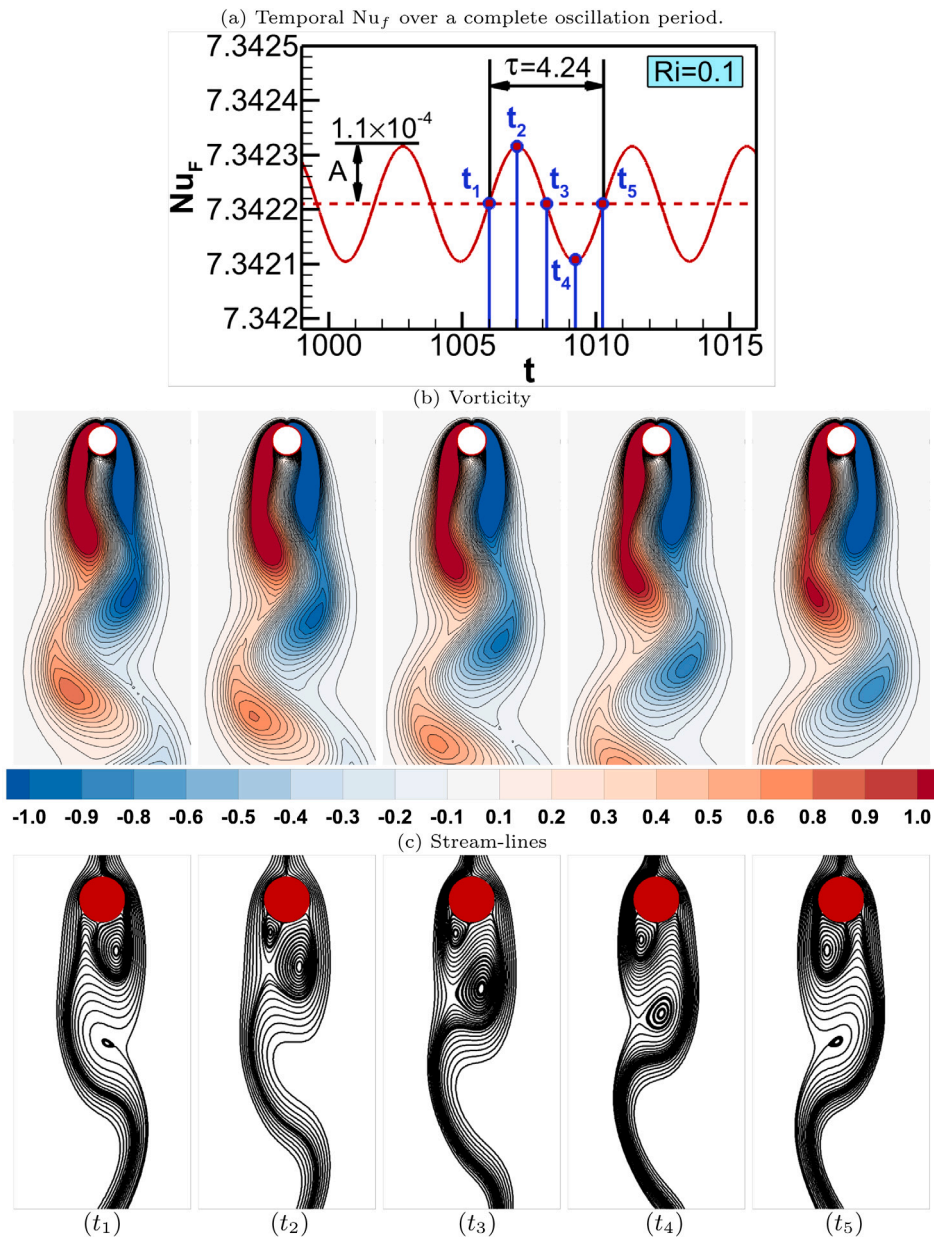
Fig. 10. (a) Transient oscillatory behaviour of Nu_f, (b) and (c) patterns of vorticity and streamlines, respectively, for five instant times over a complete oscillation period, at Re = 40 and Ri = 0.1. (For interpretation of the references to colour in this figure legend, the reader is referred to the web version of this article.)

6.1. Flow and heat transfer at Re = 100

At Re = 100, Fig. 2 displays that the usual periodic von Kármán street generated behind the unheated cylinder at Ri = 0, and its configuration is not remarkably affected by the buoyancy forces until Ri = 0.2. Beyond it, for Ri ≥ 0.2, the wake region directly behind the cylinder becomes slightly broader, and the flow fluctuations in the far downstream region becomes remarkably wider, but with lower frequency and higher amplitude. This behaviour of flow fluctuations is shown to move towards the near-wake region as Richardson number increases. This means that the strength the vortex street is decreased, but its cross-stream amplitude is increased, by increasing buoyancy. In addition, the thermal behaviour displayed in iso-therm contour maps is a clear reflection of what is happening in the flow field represented by the streamline patterns. Hence, the iso-therm waviness in the formation region and further downstream is another obvious indication of the maintenance of flow periodicity at all Richardson numbers at this

Reynolds number. Fig. 3 shows the variation of average Nusselt number (Nu_F) with time at Re = 100 and for Ri = 0 − 0.5. It can be seen that the high-frequency fluctuations of the average Nusselt number, which are precisely associated with the flow fluctuations caused by the von Kármán street, occur at all Richardson numbers. The images illustrate regular variations implying regular vortex shedding having a steady frequency and amplitude for all cases. Also, the time history exemplifies how the opposing buoyancy delays the transient period for the flow to start fluctuating. Figs. 4 and 5 show the temporal variation of average Nusselt number over a whole oscillation period with images showing the vorticity and streamlines patterns at five instants in time along this period, at Ri = 0 and 0.5, respectively. This is to show that a regular von Kármán street occurs at both Ri = 0 and 0.5, and how the buoyancy forces slightly widen the wake region. Under the opposing buoyancy effects, buoyancy acts upwards opposing the action of flow inertia. Therefore, as a result of increasing Richardson number, the flow separation points on the cylinder surface move towards the
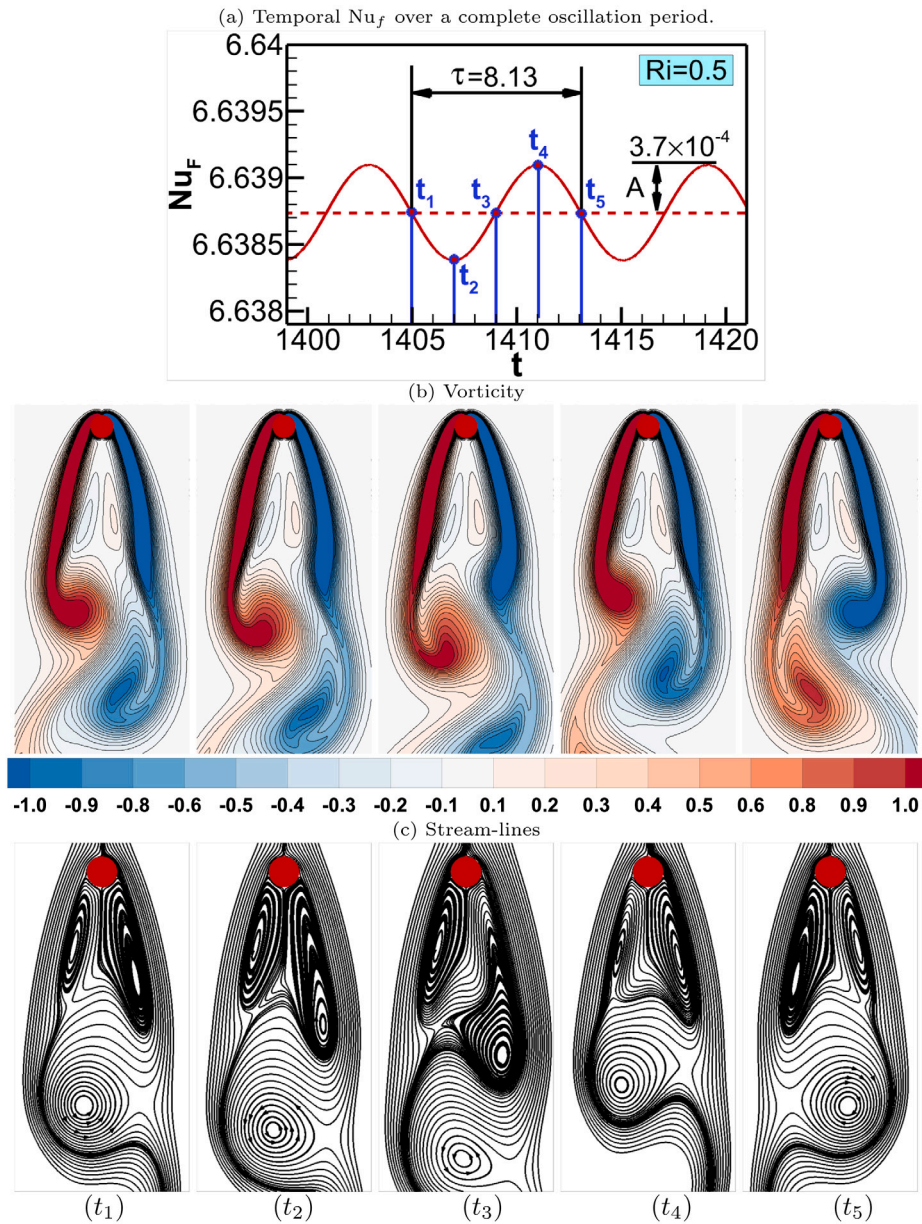
(a) Temporal Nu_f over a complete oscillation period.

(b) Vorticity

(c) Stream-lines

Fig. 11. (a) Transient oscillatory behaviour of Nu_f, (b) and (c) patterns of vorticity and streamlines, respectively, for five time instants over a complete oscillation period, at Re = 40 and Ri = 0.5. (For interpretation of the references to colour in this figure legend, the reader is referred to the web version of this article.)

forward stagnation area, triggering an untimely separation. This causes the wake to become wider, and its period to reduce. In addition, the figures demonstrate that the oscillation period (τ) and the amplitude (A) are obtained from the time variation of instantaneous average Nusselt number.

Fig. 6 displays the variation of Strouhal number (St), oscillation amplitude (A), and average Nusselt number with Richardson number at Re = 100. The Strouhal number is calculated as follows:

$$\mathrm{St} = \frac{fD}{U_\infty},\tag{18}$$

where, $f = 1/\tau$ is the oscillation frequency, which is the inverse of the period, and $U_\infty = -V_o$ is the inflow speed. Once again, the full oscillation period (τ) is obtained from the temporal variation of the instantaneous surface-average Nusselt number as shown in Figs. 4 and 5. It can be seen that as Richardson number increases from 0 to 0.5, the time for completing a full oscillation cycle increases from 2.999 to 3.399, and accordingly the value of the Strouhal number decreases from 0.3344 to 0.294, but the Nusselt number oscillation amplitude increases

from 2.24×10^{-2} to 2.64×10^{-2}. That is, the regular von Kármán street under the buoyancy effect oscillates more slowly but with larger amplitude. Also, it is obvious that the increase in Richardson number beyond a zero value leads to a considerable decrease in the average Nusselt number. In fact, increasing Richardson number at a given value of Reynolds number means increasing the Grashof number. As Grashof number increases, the flow velocity field close to the cylinder surface and the flow fluctuating on its surface slow down by the influence of buoyancy forces, resulting in a reduction in convective heat transfer.

6.2. Flow and heat transfer at Re = 40

The von Kármán street seen behind an unheated cylinder at Re = 100 transfers to a steady flow with twin attached vortices forming a near-wake recirculation zone by decreasing the Reynolds number to Re ≤ 40. However, interestingly, with heating vortical flow behaviour starts to appear in this low range of Reynolds number through the influence of buoyancy. Hence, in Fig. 7 at Re = 40, the flow begins
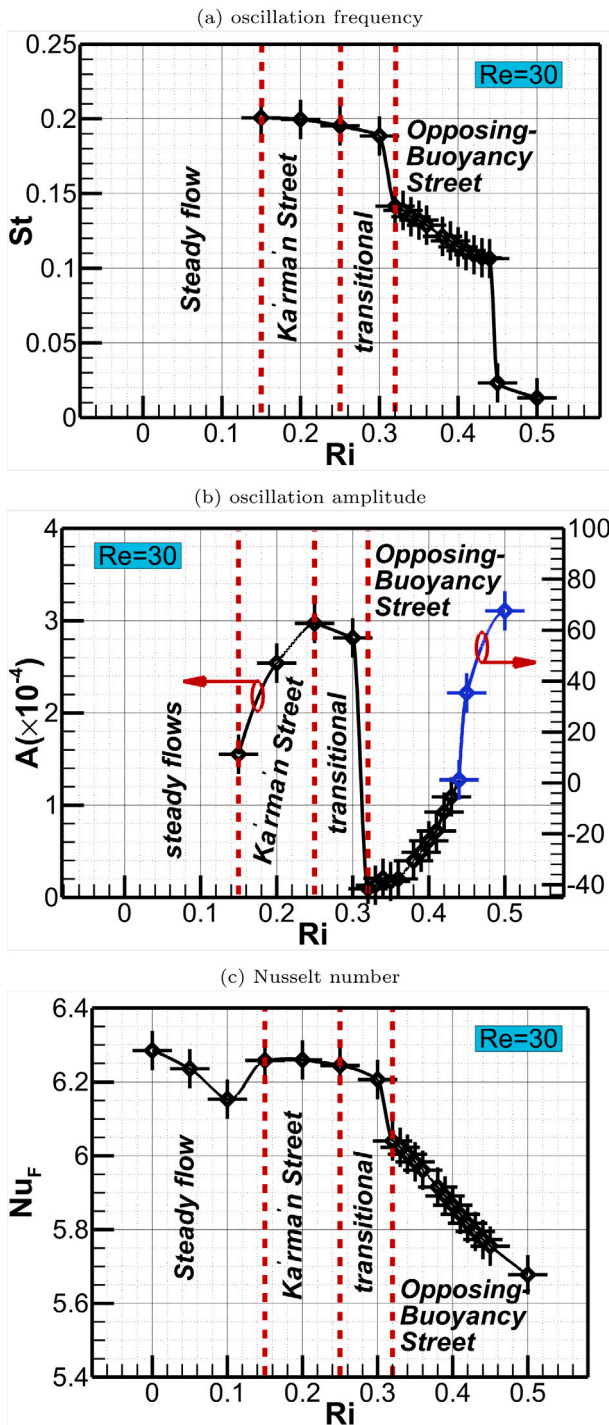
Fig. 12. Variation of (a) Strouhal number, (b) oscillation amplitude, (c) average Nusselt number, with Ri, at Re = 30.

fluctuating with a small amount of heating at Ri = 0.05. It can be seen that between $0.05 \leq Ri \leq 0.3$, the vortex street formed behind the hot cylinder is quite similar to a standard von Kármán street. It should be noticed that as Richardson increases, the wake width, which is the horizontal space between the left streamlines and the right streamlines, increases slightly, indicating to an amplification in the oscillation amplitude.

However, with more heating for Ri > 0.3, a *new* vortex street starts appearing, which is thoroughly unlike a von Kármán street. Thus, in the wake forming region, two large-scale elongated vortices are generated,

attached to the rear of the cylinder. Above the developed wake region, the streamline cross-stream extent become thinner and the streamlines meander further across the wake. This is demonstrated in Fig. 7 at Ri = 0.4 and 0.5. This kind of vortex street has not been seen before, but a similar one was reported by Noto and Sugimura (2007) for a cooling cylinder inside a vertical upward airstream, and was named as *"Cooled Vortex Street"*. Therefore, to recognise the *new* vortex street in the current study for a heated cylinder inside a vertical downward stream, we name it here as *"Buoyancy-Opposing Vortex Street"*. One can see that as Richardson number increases, the width of the wake forming region increases, and the amplitude of the meandering motion of the thin streamlines in the downstream region increases remarkably.

Fig. 8 shows the temporal variation of the average Nusselt number for different Richardson numbers $0 \leq Ri \leq 0.5$, at Re = 40. First, it can be clearly seen that the flow is steady at Ri = 0. However, for $Ri \geq 0.05$, the heat transfer is purely periodic but with different amplitudes. For more details, at Ri = 0.05, the signals begins fluctuating with a small amplitude. As Richardson number is increased until $Ri \leq 0.3$, the Nusselt number oscillation amplitude also increases. However, between $0.3 < Ri \leq 0.39$, the amplitude decreases, and then starts increasing again beyond Ri > 0.39.

To provide further insight into the strange flow behaviour for Richardson numbers between $0.3 < Ri < 0.4$, many further numerical simulations were undertaken, and as a result, the detailed variations of frequency and amplitude of flow oscillations with Richardson number are plotted in Fig. 9. It is evident that the rapid drop in the oscillation amplitude for $0.34 \leq Ri \leq 0.39$ represents the transitional region between the von Kármán street to the *"Buoyancy-Opposing Vortex Street"*. Within this region, in addition to the amplitude, the oscillation frequency also drops rapidly, and continues decreasing but more gradually after that. Therefore, it can be concluded that at Re = 40, there are four flow regimes generated behind the cylinder as Richardson number is increased from 0 to 0.5, which are characterised as follows: (a) steady flow with twin attached vortices for Ri < 0.05, (b) a regular von Kármán street for $0.05 \leq Ri \leq 0.33$, (c) transitional flow for $0.34 \leq Ri \leq 0.39$, and (d) *"Buoyancy-Opposing Vortex Street"* for Ri > 0.39. This means that the critical Richardson number for the occurrence of the *"Buoyancy-Opposing Vortex Street"* at Re = 40 is $Ri_{cr} = 0.39$. Once again, on increasing Richardson number at a given Reynolds number, the values of average Nusselt number become smaller due to the velocity reduction close to the cylinder. However, an abrupt reduction is seen to occur in the transitional region, with a more gradual one in the *"Buoyancy-Opposing Vortex Street"*. It is obvious that the average Nusselt number is functionally related to the oscillation frequency, as it has an almost similar trend.

Figs. 10 and 11 record the flow behaviour in terms of vorticity and streamlines of the von Kármán street at Ri = 0.1 and the *"Buoyancy-Opposing Vortex Street"* at Ri = 0.5, respectively, occurring at Re = 40. Note that the red–blue coloured regions of shedding from the cylinder are indeed separated shear layers. It can be seen that by increasing Richardson number from 0.1 to 0.5 at a given Reynolds number, the length of the separated shear layers increases. This is because the increasing strength of the twin wavy elongated vortices attached to the cylinder increase the downward flow velocity dropping from the separation area on the cylinder wall. Consequently, the shear layers in the wake region, which are curved in Fig. 10, become close to straight in Fig. 11. The vorticity in the wake region of the von Kármán street is larger and more asymmetric than that in the *"Buoyancy-Opposing Vortex Street"*. In addition, increasing Richardson number is seen to enlarge the angle between the separated shear layers and cylinder wall owing to the strong influence of negative buoyancy in the near-wake region. As a result, the wake width of the von Kármán street is much narrower than that of the *"Buoyancy-Opposing Vortex Street"*.
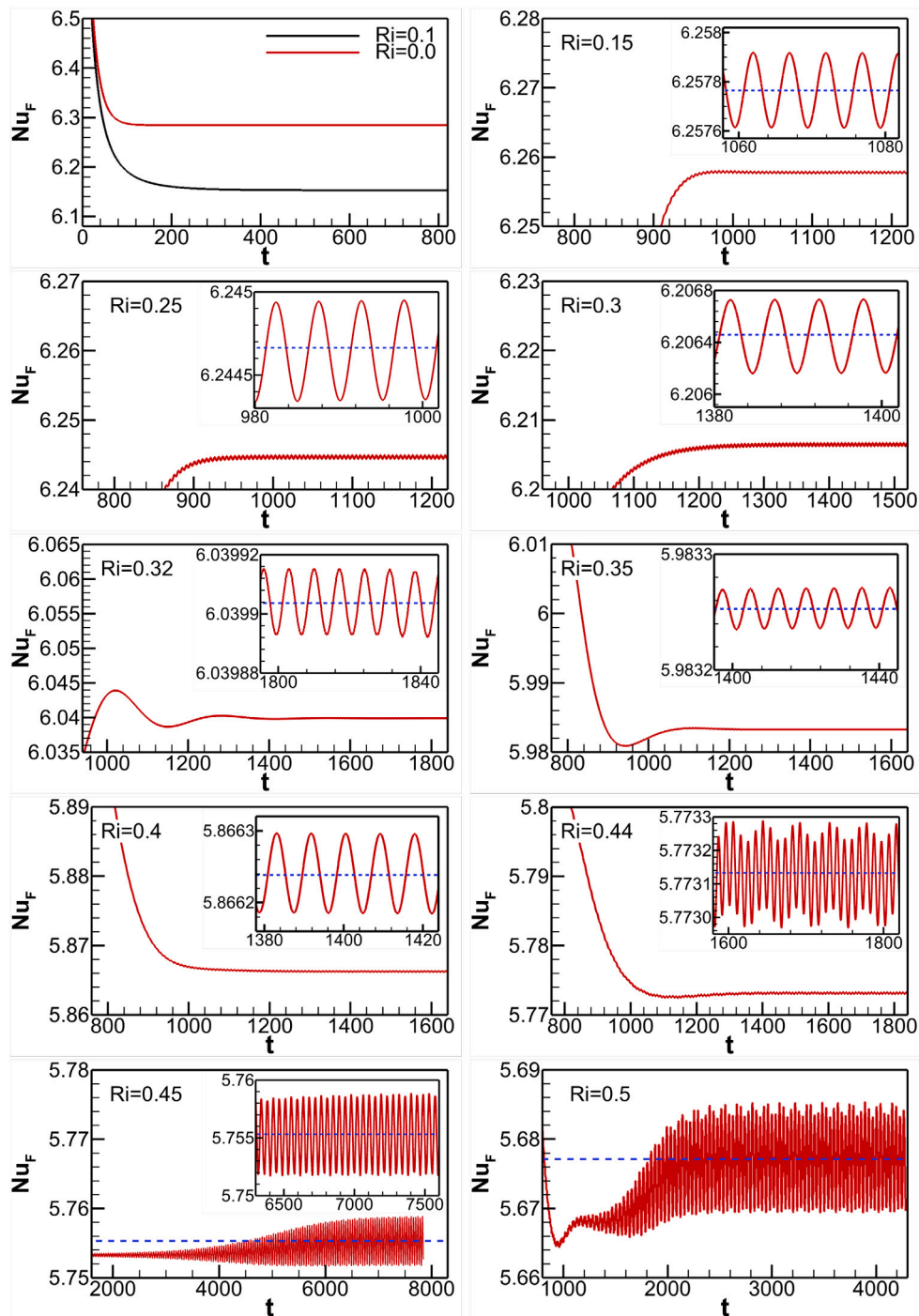
Fig. 13. Variation of Nu_F with time at Re = 30, for different Ri = 0 − 0.5.

6.3. Flow and heat transfer at Re = 30

Fig. 12 shows the variations of Strouhal number, oscillation amplitude, and average Nusselt number, with Ri, at Re = 30. We found that the steady flow region expands from Ri < 0.05 at Re = 40 to Ri < 0.15 at Re = 30. While, the range of the von Kármán street becomes narrower between 0.15 ≤ Ri ≤ 0.25 at Re = 30 instead of 0.05 ≤ Ri ≤ 0.33 at Re = 40, but with almost similar range of the transitional region. Whereas, the region of the *"Buoyancy-Opposing Vortex Street"* becomes wider to begin from Ri > 0.32 rather than Ri > 0.39 at Re = 30. This means that the critical Richardson number for obtaining the *"Buoyancy-Opposing Vortex Street"* decreases to Ri_{cr} = 0.32 at Re = 30. In addition,

interestingly, it is found that the *"Buoyancy-Opposing Vortex Street"* oscillates with significantly increased amplitude and with considerable decreased frequency as the Richardson number increases beyond Ri ≥ 0.44, and demonstrates quasi-periodic flow behaviour.

Fig. 13 displays the variation of average Nusselt number with time for different Richardson numbers Ri = 0 − 0.5, at Re = 30. The plots confirm that the flow starts oscillating at Ri ≥ 0.15. In the von Kármán street region, there is a gradual decrease in the fluctuating frequency with a sharp decrease in the fluctuating amplitude. After that, the plots confirm that there is an abrupt drop in both frequency and amplitude at Ri = 0.32 marking the beginning of the *"Buoyancy-Opposing Vortex Street"* regime. Lastly, a big jump in the oscillation amplitude and a

(a) vorticity

-1.0 -0.9 -0.8 -0.6 -0.5 -0.4 -0.3 -0.2 -0.1 0.1 0.2 0.3 0.4 0.5 0.6 0.8 0.9 1.0

(b) streamlines

(c) iso-therms

0.00 0.07 0.13 0.20 0.27 0.33 0.40 0.47 0.53 0.60 0.67 0.73 0.80 0.87 0.93 1.00
(Ri = 0.1)   (Ri = 0.15)   (Ri = 0.25)   (Ri = 0.3)   (Ri = 0.32)   (Ri = 0.4)   (Ri = 0.5)

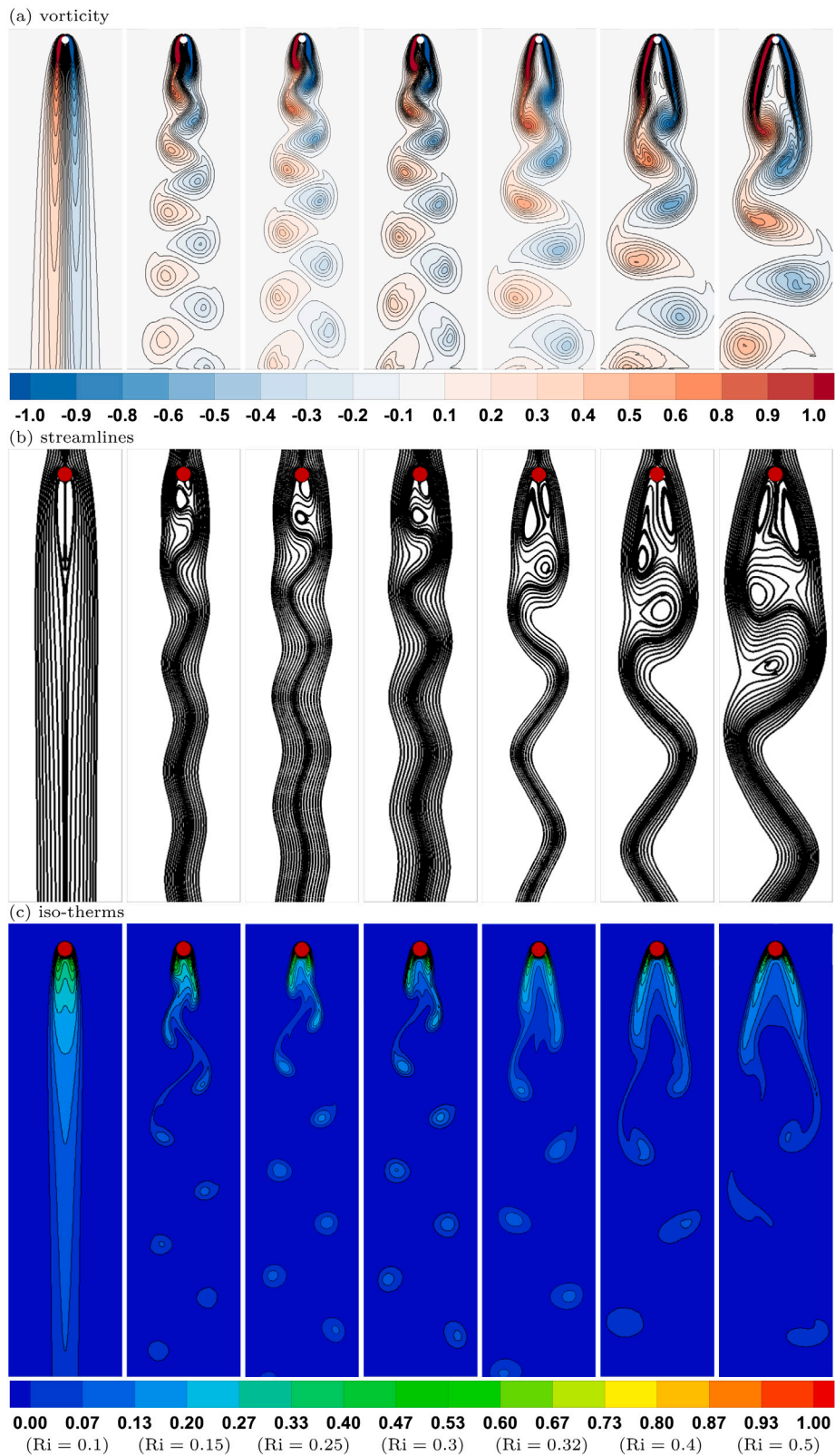**Fig. 14.** Patterns of (a) vorticity, (b) streamlines, (c) iso-therms, at Re = 30, for different Ri = 0 − 0.5.

considerable decrease in the oscillation frequency are seen beyond Ri $\geq$ 0.44, indicating transition to a chaotic flow regime. In this regime, there is a clear loss of regularity and symmetry confirming the transition from the stable wake regimes of (periodic) vortex shedding into an irregular

vortex shedding regime triggered by the strong effect of the opposing buoyancy force.

Fig. 14 shows the vorticity, streamlines, and iso-therm contours for the flow for different Ri = 0 − 0.5 at Re = 30. It is observed that
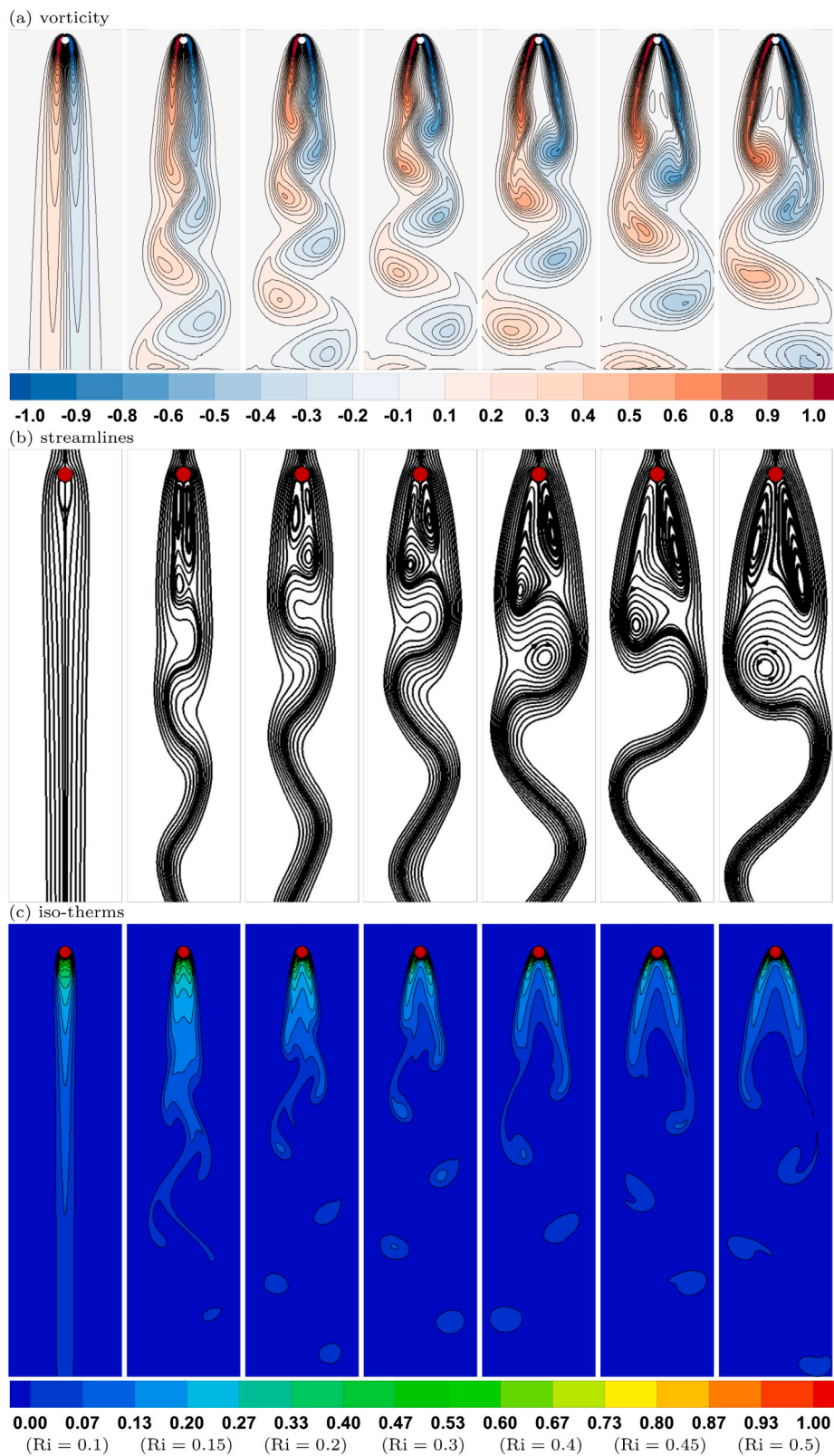
(a) vorticity

(b) streamlines

(c) iso-therms

-1.0 -0.9 -0.8 -0.6 -0.5 -0.4 -0.3 -0.2 -0.1 0.1 0.2 0.3 0.4 0.5 0.6 0.8 0.9 1.0

0.00 0.07 0.13 0.20 0.27 0.33 0.40 0.47 0.53 0.60 0.67 0.73 0.80 0.87 0.93 1.00

(Ri = 0.1)   (Ri = 0.15)   (Ri = 0.2)   (Ri = 0.3)   (Ri = 0.4)   (Ri = 0.45)   (Ri = 0.5)

Fig. 15. Patterns of (a) vorticity, (b) streamlines, (c) iso-therms, at Re = 20, for different Ri = 0 – 0.5.

the generation processes of the von Kármán street and the *"Buoyancy-Opposing Vortex Street"* at Re = 30 are qualitatively similar to those at Re = 40, except for the strong wavering chaotic motion at higher

Richardson numbers Ri $\geq$ 0.44. Thus, the double isothermal vortices behind the unheated cylinder become elongated as a result of cylinder heating. Then, with more heating, asymmetric flow behaviour is
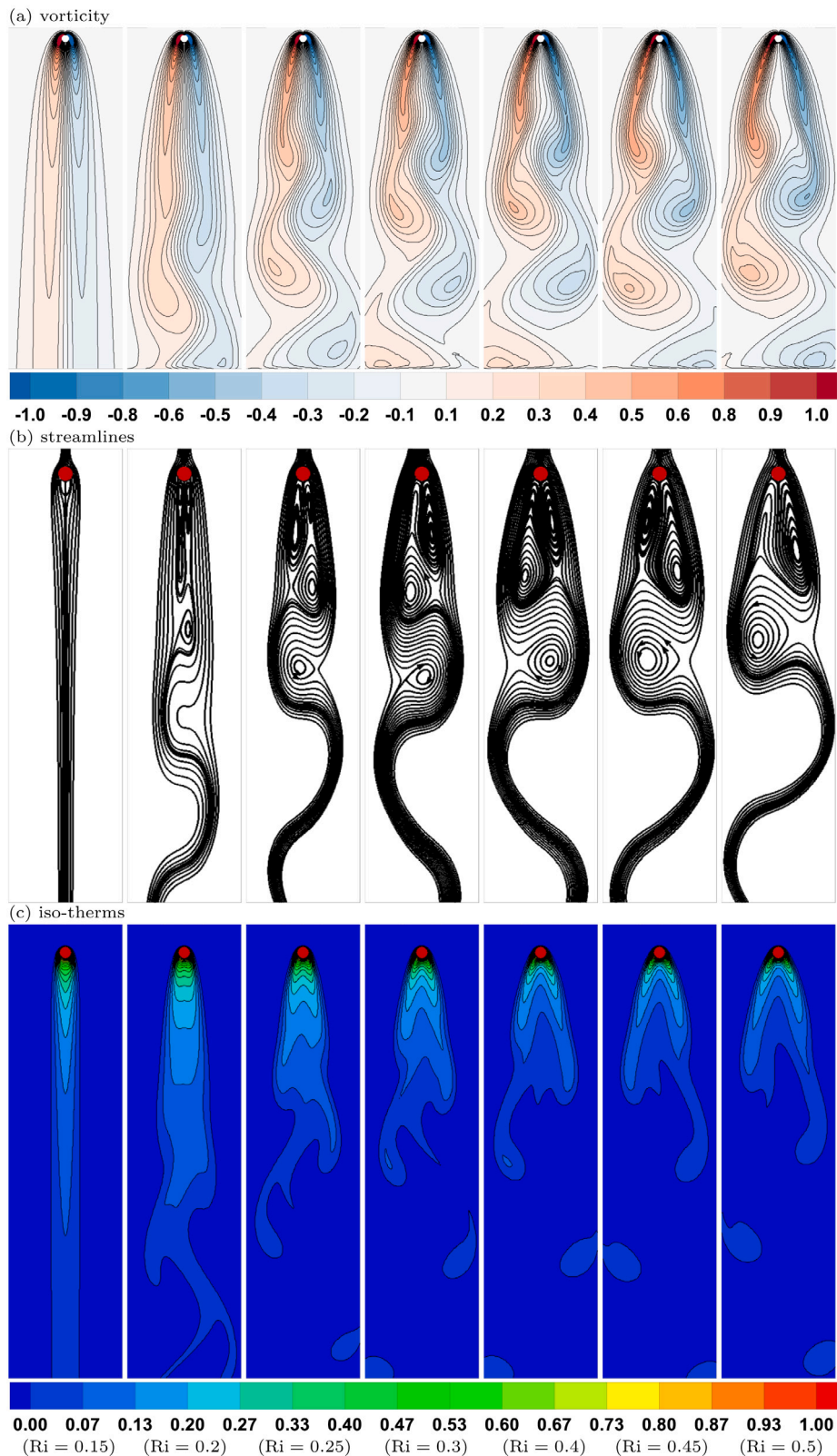
(a) vorticity

-1.0 -0.9 -0.8 -0.6 -0.5 -0.4 -0.3 -0.2 -0.1 0.1 0.2 0.3 0.4 0.5 0.6 0.8 0.9 1.0

(b) streamlines

(c) iso-therms

0.00 0.07 0.13 0.20 0.27 0.33 0.40 0.47 0.53 0.60 0.67 0.73 0.80 0.87 0.93 1.00
(Ri = 0.15)   (Ri = 0.2)   (Ri = 0.25)   (Ri = 0.3)   (Ri = 0.4)   (Ri = 0.45)   (Ri = 0.5)

Fig. 16. Patterns of (a) vorticity, (b) streamlines, (c) iso-therms, at Re = 10, for different Ri = 0 – 0.5.

generated close to the tips of the double vortices initiating ordinary vortex streets behind the heated cylinder. It is also observable that the stable vortical flow behind the heated cylinder is severely deformed and changed into chaotic flow by the buoyancy force. The images illustrate how the size and structure of the vortices, as well as their fluctuating strength alter under the thermal effects. For example, it can be seen that the flow separation points on the cylinder surface move upstream towards the front stagnation point, and the flow field impacted by the buoyancy force results in longer wakes, and the vortex streets become more unsteady.
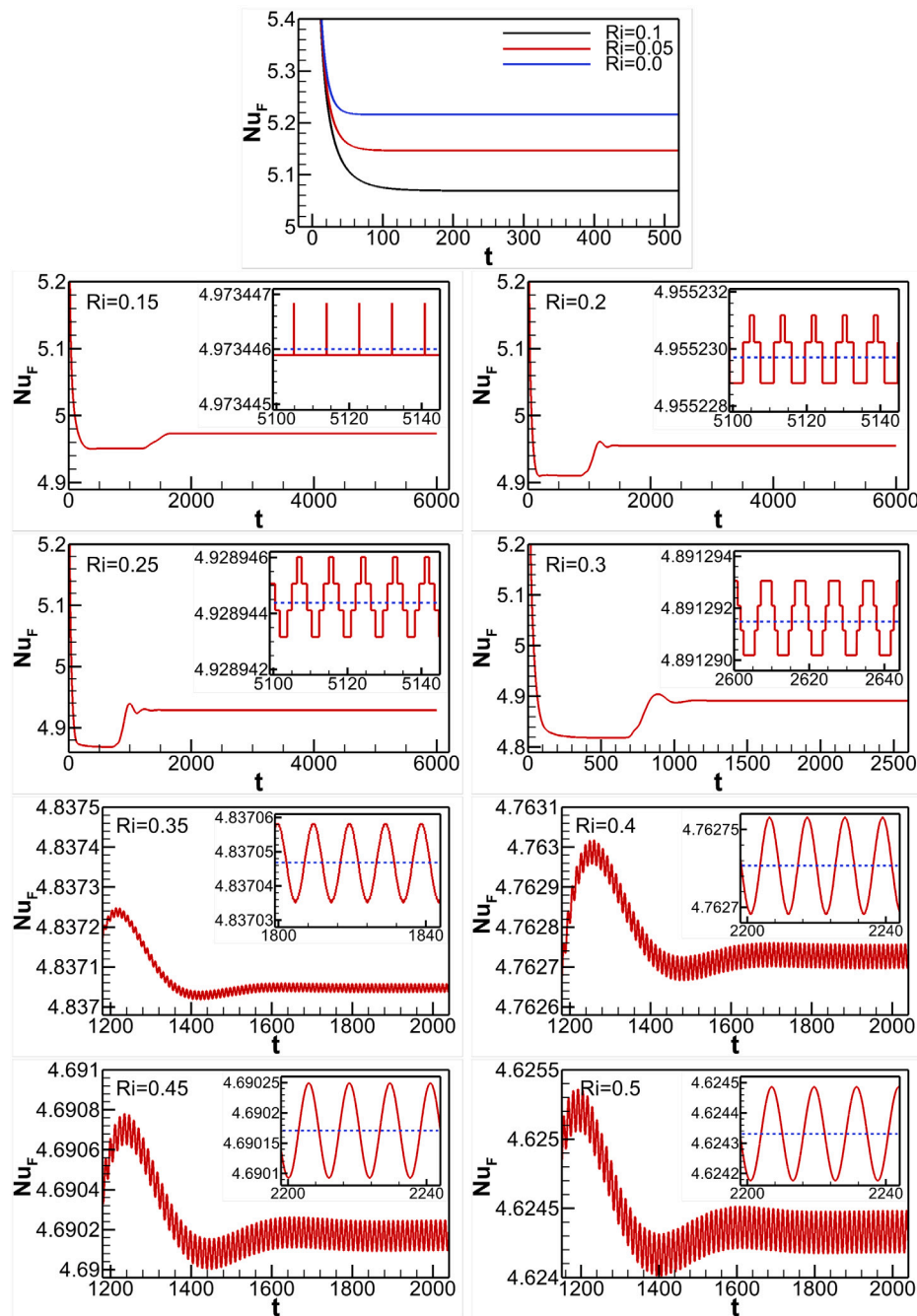
Fig. 17. Variation of Nu_F with time at Re = 20, for different Ri = 0 − 0.5.

6.4. Flow and heat transfer at Re = 20 and Re = 10

At low Reynolds numbers Re ≤ 20, we found that the usual von Kármán street is never seen in the heated wakes. That is, when the usual isothermal twin vortices that form behind the unheated cylinder are weakly heated, i.e., Ri < 0.15, these are replaced by twin elongated vortices. Further heating for this extended pair of vortices, i.e., around Ri = 0.15 at Re = 20 as shown in Fig. 15 and around Ri = 0.2 at Re = 10 as shown in Fig. 16, results in the tip regions of these vortical structures to begin to waver slightly. That is, the right and left streamlines moving around the structures are detached from each other, and the flow becomes time-dependent and asymmetric. This soft asymmetry in the wavy wake is amplified significantly by heating resulting in the *"Buoyancy-Opposing Vortex Street"* with a long formation region and robust asymmetry takes place. That is, the von Kármán street with its

short formation region never appears. This behaviour is demonstrated in Figs. 15 and 16 at Re = 20 and 10, respectively. It can be seen that the *"Buoyancy-Opposing Vortex Street"* and its meandering at Re = 10 is stronger than that at Re = 20, and both of them are stronger than those at larger Reynolds numbers previously discussed. Thus, it can be concluded that the extent of the vortex spiral in the *"Buoyancy-Opposing Vortex Street"* becomes larger as Reynolds number decreases.

Figs. 17 and 18 display the time variation of the average Nusselt number at both Re = 20 and 10, respectively, for different heating conditions Ri = 0 − 0.5. Once again, the extent of the steady flow regime enlarges and the vortex street regimes delay their appearance at the lower Reynolds numbers. It is true that the oscillatory flow behaviour appears at Ri = 0.15 when Re = 20 – same as when Re = 30. However, here at Re = 20, the oscillation is very weak and pulsatile. The plots in both figures confirm the occurrence of pulsing fluctuations
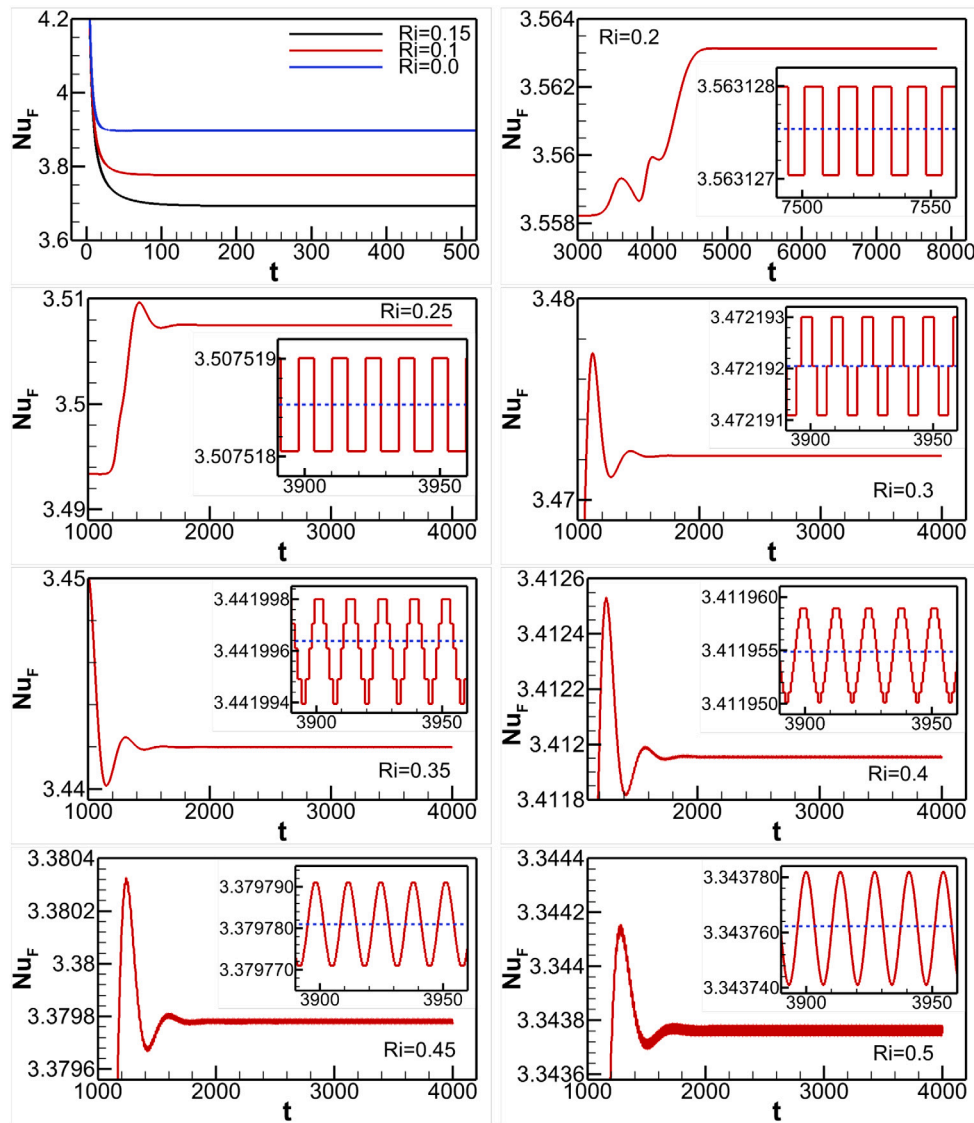
Fig. 18. Variation of Nu_F with time at $Re = 10$, for different $Ri = 0 - 0.5$.

in the wavy elongated twin vortex regime. In addition, the values of Strouhal number, oscillation amplitude and average Nusselt number are time dependent. Time-averaged values are shown in Figs. 19 and 20 at $Re = 20$ and 10, respectively. One can see that the critical Richardson number for the occurrence of the *"Buoyancy-Opposing Vortex Street"* decreases further to between $0.15 < Ri_{cr} < 0.2$ at $Re = 20$ and 10. Also, as it was demonstrated in the *"Buoyancy-Opposing Vortex Street"* region at $Re = 30$ and 40 priorly that with increasing the heating of the cylinder, the values of Strouhal and Nusselt numbers decrease, while the oscillation amplitude increases. It is clear that there is no abrupt changes in the profiles as there is only one regime controlling the flow.

7. Conclusions

In this study, comprehensive numerical simulations were conducted to investigate the unsteady mixed convective flow and thermal characteristics around an isothermally heated circular cylinder positioned within a vertically downward directed stream. An existing in-house numerical code, which is based on the spectral element method, was employed to discretise and solve the continuity, momentum and energy equations, for analysing unsteady momentum and energy transport in mixed convection regimes. The current extensive parametric investigation was performed for Reynolds numbers ranging between $Re = 10$ and

100, and Richardson numbers ranging between $Ri = 0$ and 0.5, to assess the effect of the thermal-induced buoyancy on the instantaneous flow behaviour, vortex shedding characteristics, thermal fields, and average rates of heat transfer. The simulations showed the following:

1. At $Re = 100$, the usual periodic von Kármán street observed for an unheated cylinder is preserved for all Richardson numbers investigated. Thus, with increasing Richardson number in the range $Ri = 0 - 0.5$, the Kármán street still characterises the flow; however, with lower oscillation frequency and higher cross-stream oscillation amplitude at higher Richardson number.

2. For $Re \leq 40$, a new vortex street namely, the *"Buoyancy-Opposing Vortex Street"*, appears, with distinct dissimilarities to the von Kármán street in the near wake, as it develops a robust flow asymmetry.

3. Thus, at $Re = 40$, four identified flow regimes characterise the flow behind the cylinder as Richardson number is increased from 0 to 0.5. These are described as follows: (a) steady flow with twin attached vortices, (b) an (almost) regular von Kármán street, (c) transitional flow, and (d) an *"Buoyancy-Opposing Vortex Street"*.

4. By decreasing the Reynolds number to 30, the steady flow region is seen at higher Richardson numbers, while the Ri range where the von Kármán street is seen becomes narrower, but with an almost similar
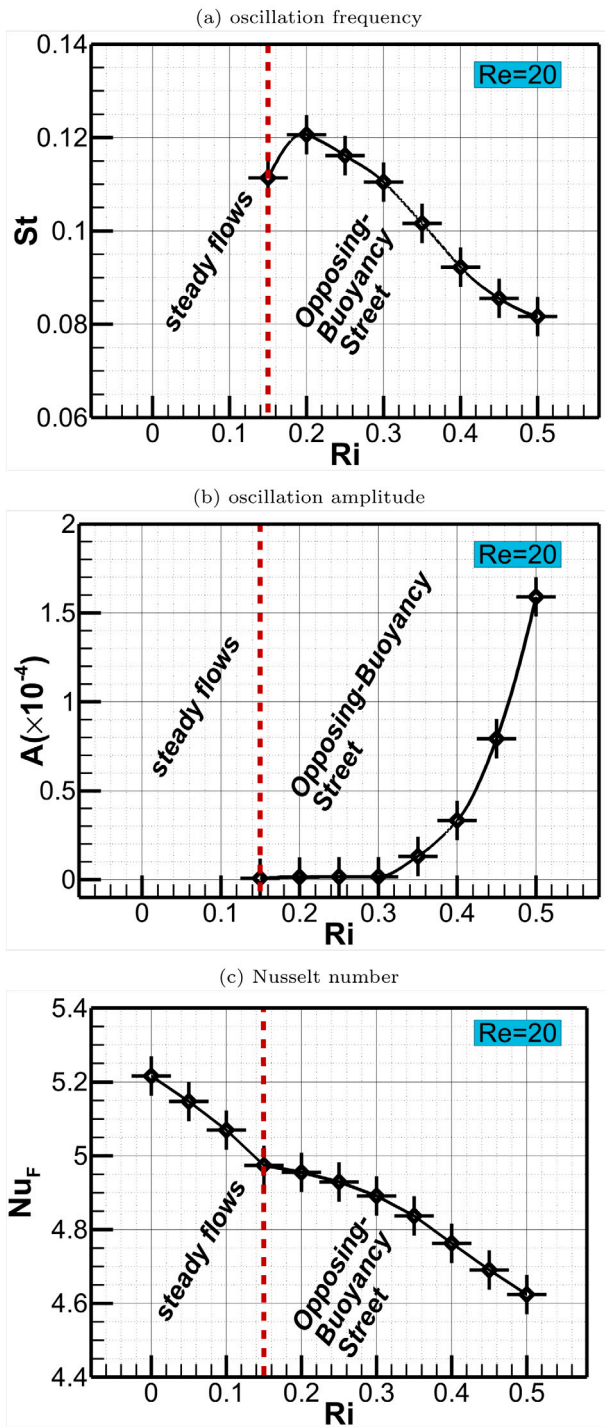
Fig. 19. Variation of (a) Strouhal number, (b) oscillation amplitude, (c) average Nusselt number, with Ri, at Re = 20.
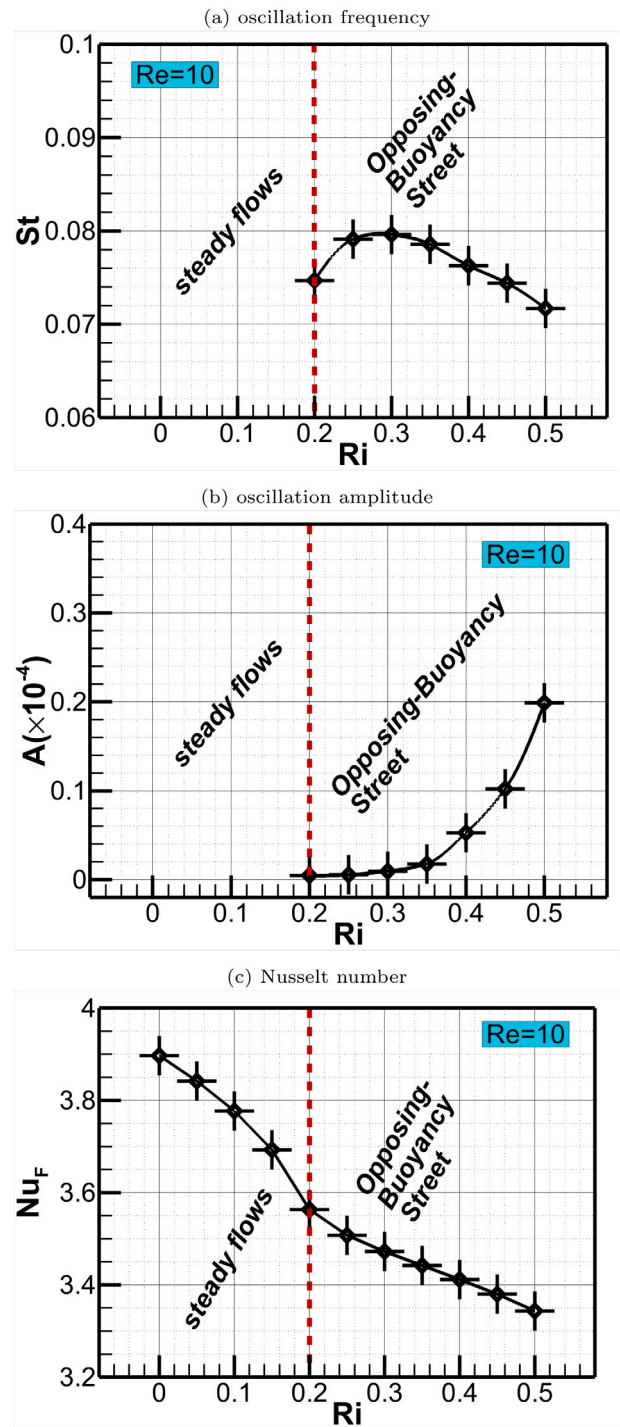

Fig. 20. Variation of (a) Strouhal number, (b) oscillation amplitude, (c) average Nusselt number, with Ri, at Re = 10.

range of the transitional region. Finally, the region of the *"Buoyancy-Opposing Vortex Street"* becomes wider with chaotic flow appearing at higher Richardson numbers.

5. At very low Reynolds numbers, Re = 20 and 10, the expansion of the steady flow region increases further, while the von Kármán street no longer appears in the heated wakes. The *"Buoyancy-Opposing Vortex Street"* continues to characterise the flow.

6. The critical Richardson number for the occurrence of the *"Buoyancy-Opposing Vortex Street"* at Re = 40 is $Ri_{cr} = 0.39$, decreasing to $Ri_{cr} = 0.32$ at Re = 30, and between $0.15 < Ri_{cr} < 0.2$ at Re = 20 and 10.

7. The average Nusselt number is a strong function of the oscillation frequency, with both showing similar trends at each Reynolds number.

8. Suggested future work

While three-dimensional transition for an unheated circular cylinder does not occur until Re = 190, the effects of thermal buoyancy may affect its onset. Thus, it is recommended that this convective heat transfer problem be investigated in the 3D form to check the impact of buoyancy effects on the flow instability in the spanwise direction.

Nomenclature

D	Cylinder diameter, (m).
Gr	Grashof number, $Gr = g.\beta.D^3.(T_h - T_o)/\nu^2$.
Nu_F	Time- and surface-average fluid Nusselt number.
P	Dimensionless fluid pressure, $P = p/\rho.\upsilon_o^2$.
Pr	Prandtl number, $Pr = \nu/\alpha$.
Re	Reynolds number, $Re = \upsilon_o.D/\nu$.
Ri	Richardson number, $Ri = Gr/Re^2$.
T	Temperature, (K).
t	Dimensionless time.
S	Cylinder circumstance, (m).
u	Horizontal velocity component, (m/s).
U	Dimensionless horizontal velocity component, $U = u/\upsilon_o$.
υ	Vertical velocity component, (m/s).
V	Dimensionless vertical velocity component, $V = \upsilon/\upsilon_o$.
x, y	Horizontal and vertical coordinates, (m).
X, Y	Dimensionless horizontal and vertical coordinates, $X = x/D, Y = y/D$.

Greek symbols

θ	Dimensionless temperature, $\theta = (T - T_o)/(T_h - T_o)$.
ρ	Fluid density, (kg/m^3).
ν	Fluid kinematic viscosity, (m^2/s).
τ	Time of one oscillation period, (s).

Subscripts

h	Hot surface.
o	Inlet condition.
n	Perpendicular direction.
s	Peripheral direction.

Declaration of competing interest

The authors declare that they have no known competing financial interests or personal relationships that could have appeared to influence the work reported in this paper.

Data availability

Data will be made available on request.

References

Al-Sumaily, G., 2014. Forced convection heat transfer from a bank of circular cylinders embedded in a porous medium. J. Heat Transf. ASME 136 (4), 042602–042602–11.

Al-Sumaily, G.F., Dhahad, H.A., Hussen, H.M., Thompson, M.C., 2020. Influence of thermal buoyancy on vortex shedding behind a circular cylinder in parallel flow. Int. J. Therm. Sci. 156, 106434.

Al-Sumaily, G., John, S., Thompson, M.C., 2012. Analysis of forced convection heat transfer from a circular cylinder embedded in a porous medium. Int. J. Therm. Sci. 51, 121–131.

Al-Sumaily, G.F., Thompson, M.C., 2013. Forced convection from a circular cylinder in pulsating flow with and without the presence of porous media. Int. J. Heat Mass Transfer 61, 226–244.

Al-Sumaily, G., Thompson, M.C., 2014. Bénard convection from a circular cylinder in a packed bed. Int. Commun. Heat Mass Transf. 54, 18–26.

Badr, H.M., 1984. Laminar combined convection from a horizontal cylinder-parallel and contra flow regimes. Int. J. Heat Mass Transfer 27 (1), 15–27.

Badr, H.M., 1985. On the effect of flow direction on mixed convection from a horizontal cylinder. Internat. J. Numer. Methods Fluids 5 (1), 1–12.

Bergere, E., Wille, R., 1972. Periodic flow phenomena. Annu. Rev. Fluid Mech. 41 (1), 313–340.

Buyruk, E., 2002. Numerical study of heat transfer characteristics on tandem cylinders, inline and staggered tube banks in cross-flow of air. Int. Commun. Heat Mass Transf. 29 (3), 355–366.

Chang, K., Sa, J., 1990. The effect of buoyancy on vortex shedding in the near wake of a circular cylinder. J. Fluid Mech. 220, 253–266.

Chatterjee, D., Mondal, B., 2012. Effect of thermal buoyancy on the two-dimensional upward flow and heat transfer around a square cylinder. Heat Transf. Eng. 33 (12), 1063–1074.

Cheng, P., 1982. Mixed convection about a horizontal cylinder and a sphere in a fluid-saturated porous medium. Int. J. Heat Mass Transfer 25 (8), 1245–1247.

Farouk, B., Guceri, S., 1982. Natural and mixed convection heat transfer around a horizontal cylinder within confining walls. Numer. Heat Transf. 5 (3), 329–341.

Gandikota, G., Amiroudine, S., Chatterjee, D., Biswas, G., 2010. The effect of aiding/opposing buoyancy on two-dimensional laminar flow across a circular cylinder. Numer. Heat Transf. A 58 (5), 385–402.

Guillén, I., Treviño, C., Martínez-Suástegui, L., 2014. Unsteady laminar mixed convection heat transfer from a horizontal isothermal cylinder in contra-flow: Buoyancy and wall proximity effects on the flow response and wake structure. Exp. Therm. Fluid Sci. 52, 30–46.

Hatanaka, K., Kawahara, M., 1995. Numerical study of vortex shedding around a heated/cooled circular cylinder by the three-step Taylor-Galerkin method. Internat. J. Numer. Methods Fluids 21, 857–867.

Hatton, A., James, D., Swire, H., 1970. Combined forced and natural convection with low-speed air flow over horizontal cylinders. J. Fluid Mech. 42 (1), 17–31.

Jain, P., Lohar, B., 1979. Unsteady mixed convection heat transfer from a horizontal circular cylinder. J. Heat Transf. Trans. ASME 101 (1), 126–131.

Karniadakis, G., Israeli, M., Orszag, S., 1991. High-order splitting methods of the incompressible Navier–Stokes equations. J. Comput. Phys. 97, 414–4430.

Karniadakis, G.E., Sherwin, S.J., 2005. Spectral/Hp Methods for Computational Fluid Dynamics. Oxford University Press, Oxford.

Laidoudi, H., Bouzit, M., 2018. The effects of aiding and opposing thermal buoyancy on downward flow around a confined circular cylinder. Period. Polytech. Mech. Eng. 62 (1), 42–50.

Leontini, J.S., Thompson, M.C., Hourigan, K., 2007. Three-dimensional transition in the wake of a transversely oscillating cylinder. J. Fluid Mech. 577, 79–104.

Nasr, K., Ramadhyani, S., Viskanta, R., 1994. Experimental investigation on forced convection heat transfer from a cylinder embedded in a packed bed. J. Heat Transf. ASME 116 (1), 73–80.

Nayak, S., Sandborn, V., 1977. Periodic heat transfer in directly opposed free and forced convection flow. Int. J. Heat Mass Transfer 20, 189–194.

Noto, K., Fujimoto, K., 2007. Numerical computation for buoyancy effect on three-dimensionality and vortex dislocation in heated wake with vertical mainstream. Numer. Heat Transf. A 51 (6), 541–572.

Noto, K., Matsumoto, R., 1987. Numerical simulation on development of the *Kármán* vortex street due to the negative buoyancy force. In: Numerical Methods in Laminar and Turbulent Flow, Vol. 5. p. 796.

Noto, K., Sugimura, S., 2007. Numerical computation of a new vortex (A Cooled Vortex Street) and its generation mechanism in a cooled circular cylinder wake at low Reynolds number. Numer. Heat Transf. A 52 (10), 875–909.

Oosthuizen, P., Madan, S., 1970. Combined convection heat transfer from horizontal cylinders in air. J. Heat Transf. Trans. ASME 92 (1), 194–196.

Oosthuizen, P., Madan, S., 1971. The effect of flow direction on combined convective heat transfer from cylinders to air. J. Heat Transf. Trans. ASME 93 (2), 240–242.

Patel, C.G., Sarkar, S., Saha, S.K., 2018. Mixed convective vertically upward flow past side-by-side square cylinders at incidence. Int. J. Heat Mass Transfer 127, 927–947.

Ryan, K., Thompson, M.C., Hourigan, K., 2005. Three-dimensional transition in the wake of bluff elongated cylinders. J. Fluid Mech. 538, 1–29.

Sáchica, D., Salcedo, E., Treviño, C., Martínez-Suástegui, L., 2022. Magnetohydrodynamic mixed convection and entropy generation analysis of Al$_2$O$_3$-water nanofluid past a confined circular cylinder. Int. J. Mech. Sci. 230, 107542.

Salcedo, E., Cajas, J.C., Treviño, C., Martínez-Suástegui, L., 2017. Numerical investigation of mixed convection heat transfer from two isothermal circular cylinders in tandem arrangement: buoyancy, spacing ratio, and confinement effects. Theor. Comput. Fluid Dyn. 31 (2), 159–187.

Saldaña, A.I., Treviño, C., Rosas, I.Y., Martínez-Suástegui, L., 2019. Experimental investigation of unsteady laminar mixed convection from a horizontal heated cylinder in contra-flow: Buoyancy and confinement effects on the three-dimensional heat transfer response. Eur. J. Mech. B Fluids 75, 165–179.

Salimipour, E., 2019. A numerical study on the fluid flow and heat transfer from a horizontal circular cylinder under mixed convection. Int. J. Heat Mass Transfer 131, 365–374.

Sharma, A., Eswaran, V., 2004. Effect of aiding and opposing buoyancy on the heat and fluid flow across a square cylinder at Re=100. Numer. Heat Transf. A 45 (6), 601–624.

Sharma, A., Eswaran, V., 2005. Effect of channel-confinement and aiding/opposing buoyancy on the two-dimensional laminar flow and heat transfer across a square cylinder. Int. J. Heat Mass Transfer 48 (25–26), 5310–5322.

Sheard, G.J., Thompson, M.C., Hourigan, K., 2003. From spheres to circular cylinders: The stability and flow structures of bluff ring wakes. J. Fluid Mech. 492, 147–180.

Singh, S., Biswas, G., Mukhopadhyay, A., 1998. Effect of thermal buoyancy on the flow through a vertical channel with a built-in circular cylinder. Numer. Heat Transf. A 34 (7), 769–789.

Singh, S.K., Panigrahi, P.K., Muralidhar, K., 2007. Effect of buoyancy on the wakes of circular and square cylinders: a schlieren-interferometric study. Exp. Fluids 43 (1), 101–123.

Thompson, M.C., Hourigan, K., Cheung, A., Leweke, T., 2006. Hydrodynamics of a particle impact on a wall. Appl. Math. Model. 30, 1356–1369.

Thompson, M.C., Hourigan, K., Sheridan, J., 1996. Three-dimensional instabilities in the wake of a circular cylinder. Exp. Therm Fluid Sci. 12, 190–196.

Williamson, C., 1996. Vortex dynamics in the cylinder wake. Annu. Rev. Fluid Mech. 28 (1), 477–539.